Draft version November 4, 2022
Typeset using LaTeX default style in AASTeX63

The Photospheric Imprints of Coronal Electric Currents

Brian T. Welsch[1]

[1] *Natural & Applied Sciences, University of Wisconsin-Green Bay, 2420 Nicolet Drive, Green Bay, WI 54311, USA*

ABSTRACT

Flares and coronal mass ejections are powered by magnetic energy stored in coronal electric currents. Here, we explore the nature of coronal currents in observed and model active region (ARs) by studying manifestations of these currents in photospheric vector magnetograms. We employ Gauss's separation method, recently introduced to the solar physics literature, to partition the photospheric field into three distinct components, each arising from a separate source: (i) currents passing through the photosphere, (ii) currents flowing below it, and (iii) currents flowing above it. We refer to component (iii) as the photospheric imprint of coronal currents. In both AR 10930 and AR 11158, photospheric imprints exhibit large-scale, spatially coherent structures along these regions' central, sheared polarity inversion lines (PILs) that are consistent with coronal currents flowing horizontally above these PILs, similar to recent findings in AR 12673 by Schuck et al. (2022). We find similar photospheric imprints in a simple model of a non-potential AR with known currents. We find that flare-associated changes in photospheric imprints in AR 11158 accord with earlier reports that near-PIL fields become more horizontal, consistent with the "implosion" scenario. We hypothesize that this evolution effectively shortens, in an overall sense, current-carrying coronal fields, leading to decreased inductive energy (DIE) in the coronal field. We further hypothesize that, in the hours prior to flares, parts of the coronal field slowly expand, in a process we deem coronal inflation (CI) — essentially, the inverse of the implosion process. Both of these hypotheses are testable with non-potential coronal field extrapolations.

1. INTRODUCTION

Despite decades of study, the physical processes that generate solar flares and coronal mass ejections (CMEs) are not fully understood. A core concept, referred to as the storage-and-release paradigm, is that these events are powered by the release of magnetic energy stored in coronal electric currents; see, e.g., the discussion of "storage models" by Forbes (2000). Accordingly, electric currents flowing through the solar corona play key roles in determining when and where these magnetically-driven events occur. Indeed, if a coronal magnetic field lacked currents (and was thus curl-free by Ampère's law, $\mu_0 \mathbf{J} = \nabla \times \mathbf{B}$), then we expect flares and CMEs would not occur. Because a curl-free vector field can be represented as the gradient of a scalar potential, a current-free magnetic field is often referred to as "potential," and current-carrying fields are often called "non-potential."

The presence of currents in observed photospheric, chromospheric, and coronal fields can be inferred from significant deviations between the observed fields and potential-field models. For a given magnetic-field boundary condition (an issue discussed in detail below), a potential field is unique, so any mismatch between observations and the potential model implies that currents are present. Schrijver et al. (2005) compared observed coronal extreme ultraviolet (EUV) loops with field lines in potential models of the coronal field in several dozen active regions (ARs), and found flares to be significantly more likely in non-potential ARs. In AR magnetograms (i.e., 2D maps of the 3-component magnetic field), non-potential photospheric fields are frequently observed near polarity inversion lines (PILs, where the vertical component of the photospheric magnetic field changes sign): near-PIL fields are often sheared (e.g., Moore et al. 1987), possessing a strong shear component that runs *along* the PIL, rather than *across* the PIL as in generic potential fields. Large flares and eruptions invariably start in the atmosphere immediately above strongly sheared PILs. Filaments and helmet streamers, which can erupt as CMEs, also exhibit non-potential magnetic structures that imply the presence of electric currents, such as field-aligned H-α fibrils in filaments whose orientations are inconsistent with potential-field orientations (e.g., Martin 1998), and above-limb rings of enhanced linear polarization consistent with flux ropes viewed in cross section (e.g., Dove et al. 2011).

Since currents play key roles in determining when, where, and how magnetic energy is released in flares and CMEs, understanding these events requires addressing a fundamental question: What is the structure of coronal electric

currents, and how do they evolve? Unfortunately, observations provide only limited information about $\mathbf{B}$ in the corona — e.g., the line-of-sight-integrated transverse component of $\mathbf{B}$ above the limb (e.g., Lin et al. 2004; Tomczyk et al. 2008; Dove et al. 2011), or field strength $|\mathbf{B}|$ from radio gyrosynchrotron observations (e.g., Brosius & White 2006). (We remark that the Frequency-Agile Solar Radiotelescope [FASR, Bastian et al. 2019], if built, should greatly improve observational characterization of coronal magnetic fields.) Hence, the distribution of electric currents in the corona ($\mathbf{J}$ as a function of space) cannot be directly measured with present capabilities.

Consequently, modeling of the coronal magnetic field is essential for the study of the structure of coronal currents. One common technique for such modeling is extrapolation of the coronal magnetic fields from photospheric vector magnetograms, under the assumption that the Lorentz force in the coronal field vanishes, $\mathbf{J} \times \mathbf{B} = 0$. For nonzero currents, this implies

$$\nabla \times \mathbf{B} = \alpha \mathbf{B} \ , \tag{1}$$

where, in the general case, α varies in space. When α is a function of position, solutions of this equation are referred to as non-linear, force-free fields (NLFFFs). Several methods for finding NLFFFs have been developed; for a review, see, e.g., Wiegelmann & Sakurai (2012). A factor limiting the strength of inferences about coronal fields based on NLFFF fields is that the field on the bottom boundary of such models typically exhibits substantial discrepancies with observed fields (e.g., Wheatland & Leka 2011). While some amount of mismatch between NLFFF models' boundary fields and data is understandable — due to measurement errors and the non-force-free nature of photospheric fields (e.g., Metcalf et al. 1995) — model-data discrepancies are often large and "in excess of nominal uncertainties in the data" (DeRosa et al. 2015).

A recent, exciting development in the study of solar magnetic fields promises progress in understanding coronal currents: the first-of-its-kind application of Gauss's separation method — a technique with a long heritage in terrestrial and planetary magnetism (e.g., Olsen et al. 2010) — to photospheric vector magnetograms of solar active regions by Schuck et al. (2022). We discuss this approach in detail in Section 2 below, but the key idea of the Gauss separation method is straightforward: part of the observed magnetic field at the photosphere can be *unambiguously* attributed to currents flowing above the photosphere. Mathematically, in Cartesian coordinates with the photosphere at $z = 0$, the observed photospheric field $\mathbf{B}(x, y, 0)$ can be uniquely partitioned into three components,

$$\mathbf{B}(x, y, 0) = \mathbf{B}_h^{\rm rot}(x, y, 0) + \mathbf{B}^{<}(x, y, 0) + \mathbf{B}^{>}(x, y, 0) \ , \tag{2}$$

where: $\mathbf{B}_h^{\rm rot}(x, y, 0)$, the rotational component of the horizontal photospheric field, is due to currents, $J_z(x, y, 0)$, that pass through the photosphere; $\mathbf{B}^{<}(x, y, 0)$ is due to currents $\mathbf{J}^{<}$ interior to the photosphere; and $\mathbf{B}^{>}(x, y, 0)$ is due to currents $\mathbf{J}^{>}$ above it. For simplicity, we call all currents flowing above the photosphere "coronal," whether they flow in the chromosphere, transition region, or corona, and we refer to $\mathbf{B}^{>}(x, y, 0)$ as the **photospheric imprint** of coronal currents. While many models of coronal magnetic fields have assumed that coronal currents only affect the horizontal photospheric field, Gauss's method reveals that these currents also produce a significant part of the observed $B_z(x, y, 0)$ (Schuck et al. 2022, and below). We remark that Gauss's separation method makes no assumption about photospheric fields being force-free.

This paper considers the structure of coronal currents and the nature of energy storage and release in flares. Much of our analysis builds upon the recent study by Schuck et al. (2022), who took the key step of applying Gauss's separation algorithm (Olsen et al. 2010; Backus 1986) to solar fields. Because this approach is new within solar physics, we begin by discussing the decomposition in Equation (2) in the next Section. Then, in Section 3, we investigate the structure of photospheric imprints in two flare-productive regions, NOAA ARs 10930 and 11158, and a simple model of a non-potential, quadrupolar AR configuration. Next, in Section 4, we investigate flare-associated changes in light of the decomposition in Equation (2), and discuss a hypothesis about the release of inductive magnetic energy in flares — the Decrease in Inductive Energy model. In Section 5, we discuss our key findings, their possible applications, and directions for future work. We also introduce the Coronal Inflation hypothesis, and suggest observational tests of it.

2. DECOMPOSITIONS OF PHOTOSPHERIC $\mathbf{B}$

Gauss (1839) presented a method to partition the magnetic field on a spherical surface into two components, each with a distinct source: either currents interior to the surface, or exterior to it. (See Glassmeier & Tsurutani (2014) for a modern translation.) Gauss's approach assumed that no currents flowed *across* the surface, but Backus (1986) presented a generalization of Gauss's approach to cases when currents cross the surface, enabling the decomposition

shown in Equation (2). (See the first few pages of Olsen et al. (2010) for a brief review of the spherical version of that decomposition.)

Here, we present an approach for the Cartesian version of the decomposition in Equation (2). We choose to represent the observed photospheric field as

$$\mathbf{B}(x,y,0) = \nabla \times T(x,y)\,\hat{\mathbf{z}} - \nabla\chi^{-}(x,y,0) - \nabla\chi^{+}(x,y,0)\ , \tag{3}$$

where: $T(x,y)$ is a stream function whose curl gives the horizontal field's rotational component, $\mathbf{B}_h^{\rm rot}(x,y,0)$; $\mathbf{B}^{<}(x,y,z) = -\nabla\chi^{-}(x,y,z)$ is the magnetic field at and above the photosphere ($z \geq 0$) due to interior currents ($\mathbf{J}^{<}$) flowing in $z < 0$; and $\mathbf{B}^{>}(x,y,z) = -\nabla\chi^{+}(x,y,z)$ is the magnetic field at and below the photosphere ($z \leq 0$) due to exterior (coronal) currents ($\mathbf{J}^{>}$) flowing in $z > 0$. We assume a zero-thickness photosphere, meaning horizontal currents must either be above or below it. (Although some magnetograph spectral lines form over a finite height range [e.g., ∼300 km for Fe I 6173Å; Fleck et al. 2011], this zero-thickness assumption is a good approximation for the structures that are our focus, which extend over a few Mm or more.) Thus, the only nonzero current at the photosphere is vertical. Ampère's law, with the vertical component of the curl of Equation (3), gives

$$\hat{\mathbf{z}}\cdot(\nabla\times\mathbf{B})|_{z=0} = -\nabla_h^2 T(x,y) = \mu_0 J_z(x,y,0)\ , \tag{4}$$

a 2D Poisson equation for $T(x,y)$, where the horizontal gradient is $\nabla_h \equiv (\partial_x, \partial_y, 0)^T$. (The curls of the gradient terms in Equation (3) vanish.)

The horizontal photospheric field produced by currents at $z \neq 0$ must have no curl on $z = 0$. This irrotational part of $\mathbf{B}_h(x,y,0)$ can thus be expressed as the horizontal gradient of a scalar potential, $\mathbf{B}_h^{\rm irrot}(x,y,0) = -\nabla_h\chi(x,y)$. From the Biot-Savart law, any $\mathbf{B}$ depends linearly on in its source currents, meaning $\chi(x,y) = \chi^{-}(x,y,0) + \chi^{+}(x,y,0)$. Taking the horizontal divergence of equation (3) gives

$$(\nabla_h\cdot\mathbf{B}_h) = -\nabla_h^2\chi^{-} - \nabla_h^2\chi^{+}\ . \tag{5}$$

(Because the divergence of a curl vanishes, the rotational component of $\mathbf{B}_h(x,y,0)$, from the stream-function term, does not contribute here.)

The Biot-Savart law also implies that $J_z(x,y,0)$ produces no vertical field at the photosphere, so $B_z(x,y,0)$ is entirely due to currents at $z \neq 0$. Hence, at $z = 0$, $B_z(x,y,0)$ can be represented with gradients of $\chi^{\pm}$,

$$B_z(x,y,0) = -\partial_z\chi^{-} - \partial_z\chi^{+}\ . \tag{6}$$

Note a key implication of Equation (6): part of the observed vertical field at the photosphere is due to coronal currents. Because magnetic fields are divergence-free, $\nabla\cdot\mathbf{B}^{<} = \nabla\cdot\mathbf{B}^{>} = 0$, and the potentials $\chi^{\pm}$ both obey the 3D Laplace's equation,

$$-\nabla^2\chi^{-} = 0\ , z\in[0,\infty)\ , \tag{7}$$

$$\nabla^2\chi^{+} = 0\ , z\in(-\infty,0]\ . \tag{8}$$

If we were solving for a single potential that solved Laplace's equation, Equation (5) would form a Dirichlet boundary condition for that potential, and Equation (6) would form a Neumann condition for that potential (Welsch & Fisher 2016). In general, both cannot be satisfied by a single solution to Laplace's equation (e.g., Jackson 1975). Here, however, we have two potential functions and two boundary conditions.

We now digress to review, briefly, how currents above and below the photosphere affect the photospheric field components that enter these boundary conditions. Our starting point is the differential form of the Biot-Savart law,

$$d\mathbf{B}(\mathbf{r}) = \frac{\mu_0}{4\pi}\frac{\mathbf{J}(\mathbf{r}_s)\times(\mathbf{r}-\mathbf{r}_s)}{|\mathbf{r}-\mathbf{r}_s|^3}dV\ , \tag{9}$$

where $\mathbf{r}_s$ is the coordinate vector of a source point with an infinitesimal current-carrying segment $\mathbf{J}(\mathbf{r}_s)dV$ that produces a magnetic field $d\mathbf{B}$ at the point with coordinate vector $\mathbf{r}$. The current density can be decomposed into horizontal and vertical components, $\mathbf{J} = \mathbf{J}_h + J_z\,\hat{\mathbf{z}}$.

We first consider the contribution of $\mathbf{J}_h(x,y,z)$ to $\mathbf{B}(x,y,0)$. Figure 1 illustrates components of the magnetic field produced at the photosphere due to horizontal currents above and below it. The magnetic field vectors' colors match the

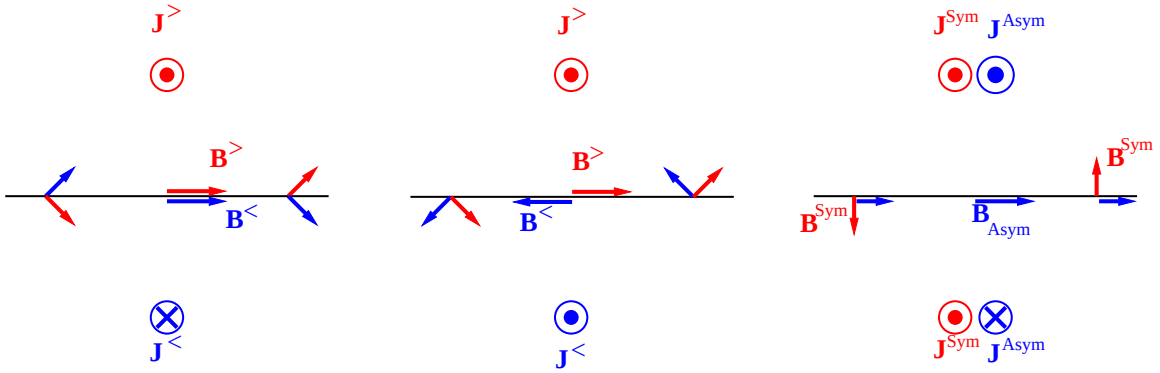

Figure 1. *Left: A current above the phtotosphere,* $\mathbf{J}^{>}$ *(red vector pointing toward the reader) produces a magnetic field,* $\mathbf{B}^{>}$*, shown by the red vectors lying in the plane of the figure. (In this and other panels, all magnetic field vectors' colors match the color of their source currents.) An equal but opposite current below the photosphere,* $\mathbf{J}^{<}$ *(blue vector pointing away from the reader), produces a magnetic field,* $\mathbf{B}^{<}$*, shown by blue vectors lying in the plane of the figure. These antisymmetric currents produce no normal field at the photosphere. Adopting a coordinate system with* $+x$ *to the right in this figure, notice that these currents produce a nonzero* $\partial_x B_x$ *at the photosphere, implying that* $(\nabla_h \cdot \mathbf{B}_h) \neq 0$*. Middle: Symmetric currents above and below the photosphere produce a normal magnetic field at the photosphere, but no horizontal field there. Right: A coronal current without a matching sub-photospheric counterpart can be represented as the sum of symmetric and anti-symmetric currents, with* $|\mathbf{J}^{\rm Sym}| = |\mathbf{J}^{\rm Asym}|$*; the* $\mathbf{J}$ *vectors shown are meant to be co-spatial. Such a configuration produces both normal and horizontal photospheric fields.*

color of their source currents. A horizontal current flowing in the corona will produce a magnetic field with both normal and horizontal components at the photosphere. As the figure's left panel illustrates, for the special case of horizontal currents that are antisymmetric across the photosphere, no normal magnetic field is produced at the photosphere. This property of antisymmetric, mirror/image currents has been exploited in coronal magnetic field modeling (e.g., Sakurai 1981; Wheatland 2007). The middle panel shows the situation with currents that are symmetric across the photosphere: in this case, a normal field is produced at the photosphere, but no horizontal field is produced there. Sezginer & Chew (1990) present formalism that can be used to extend the concepts of symmetric and antisymmetric horizontal currents in Cartesian geometry to spherical geometry. The right panel, in which $|\mathbf{J}^{\rm Sym}| = |\mathbf{J}^{\rm Asym}|$ and the $\mathbf{J}$ vectors are meant to be co-spatial, shows a configuration with nonzero current in the corona, but zero current below it. The logic used in the right-panel example can be applied for any current at any point, demonstrating that an arbitrary current density can be represented as the sum of symmetric and antisymmetric parts. In this last, generic case, horizontal currents produce both horizontal and vertical magnetic fields at the photosphere.

Next, we consider the contributions to $\mathbf{B}(x, y, 0)$ from $J_z(x, y, z)$ when $z \neq 0$. The cross product in the numerator of Equation (9) implies that the vertical component of the current at a given source point does not produce any vertical magnetic field at the photosphere. A radial current segment does produce a horizontal photospheric field, but the horizontal photospheric field produced by a current system that does not penetrate the photosphere must be irrotational, per the integral form of Ampère's law ($\mu_0 I_{\rm enc} = \oint \mathbf{B} \cdot d\boldsymbol{\ell}$).

These examples demonstrate that, outside of special cases, horizontal currents above and below the photosphere produce both (i) vertical fields and (ii) horizontal, irrotational fields there. Vertical currents off the photosphere also produce horizontal fields there.

We now proceed to solve for $\chi^{\pm}$ using a Fourier method; after presenting this approach, we discuss other solution methods. Mathematically, we have two equations, (5) and (6), that give boundary conditions in terms of observable quantities for two unknown potential functions, χ^{+} and χ^{-}, that each satisfy Laplace's equation. The potentials $\chi^{\pm}$ can be expressed in terms of Fourier transforms as

$$\chi^{\pm}(x, y, z) = \frac{1}{(2\pi)^2} \int_{-\infty}^{+\infty} \mathrm{d}k_x \int_{-\infty}^{+\infty} \mathrm{d}k_y \, \tilde{\chi}^{\pm}(\mathbf{k}) \mathrm{e}^{\mathrm{i}k_x x + \mathrm{i}k_y y \pm k_h z} \ . \tag{10}$$

For each potential to solve Laplace's equation, we require $k_h \equiv |\sqrt{k_x^2 + k_y^2}|$.

In terms of these Fourier transforms, Equation (6) becomes

$$B_z(x,y) = -\partial_z\chi^+|_{z=0} - \partial_z\chi^-|_{z=0} \tag{11}$$

$$= \frac{1}{(2\pi)^2}\int_{-\infty}^{+\infty}\mathrm{d}k_x\int_{-\infty}^{+\infty}\mathrm{d}k_y\,(\tilde{\chi}^-(k_x,k_y) - \tilde{\chi}^+(k_x,k_y))\,k_h\,e^{\mathrm{i}k_x x+\mathrm{i}k_y y}\ . \tag{12}$$

Notice that the z-dependence of χ^- and χ^+ differs: the former decays upward and the latter decays downward, meaning this condition involves a *difference* of their spectral functions. Denoting the Fourier transform of $B_z(x,y,0)$ as $\tilde{B}_z$, we have

$$\tilde{\chi}^-(k_x,k_y) - \tilde{\chi}^+(k_x,k_y) = \frac{\int_{-\infty}^{+\infty}\mathrm{d}x\int_{-\infty}^{+\infty}\mathrm{d}y\,B_z(x,y)\mathrm{e}^{-\mathrm{i}k_x x-\mathrm{i}k_y y}}{k_h} = \frac{\tilde{B}_z(k_x,k_y)}{k_h}\ . \tag{13}$$

In terms of the Fourier transforms of $\chi^\pm$, Equation (5) becomes

$$\nabla_h\cdot\mathbf{B}_h(x,y) = \nabla_h\cdot\left(\frac{1}{(2\pi)^2}\int_{-\infty}^{+\infty}\mathrm{d}k_x\int_{-\infty}^{+\infty}\mathrm{d}k_y\,\tilde{\mathbf{B}}_h(k_x,k_y)\mathrm{e}^{-\mathrm{i}k_x x-\mathrm{i}k_y y}\right) \tag{14}$$

$$= \frac{1}{(2\pi)^2}\int_{-\infty}^{+\infty}\mathrm{d}k_x\int_{-\infty}^{+\infty}\mathrm{d}k_y\,\mathrm{i}\mathbf{k}_h\cdot\tilde{\mathbf{B}}_h(k_x,k_y)\mathrm{e}^{-\mathrm{i}k_x x-\mathrm{i}k_y y} \tag{15}$$

$$= \frac{1}{(2\pi)^2}\int_{-\infty}^{+\infty}\mathrm{d}k_x\int_{-\infty}^{+\infty}\mathrm{d}k_y\,(\tilde{\chi}^+(k_x,k_y) + \tilde{\chi}^-(k_x,k_y))(k_x^2+k_y^2)\mathrm{e}^{\mathrm{i}k_x x+\mathrm{i}k_y y}\ , \tag{16}$$

where $\tilde{\mathbf{B}}_h(k_x,k_y)$ is the 2D Fourier transform of $\mathbf{B}_h(x,y)$. The previous two equations imply that

$$\tilde{\chi}^+(k_x,k_y) + \tilde{\chi}^-(k_x,k_y) = \frac{\mathrm{i}\mathbf{k}_h\cdot\tilde{\mathbf{B}}_h(k_x,k_y)}{k_h^2}\ . \tag{17}$$

While Equation (13) involved a difference of $\tilde{\chi}^+$ and $\tilde{\chi}^-$, Equation (17) involves their *sum*. This is a key aspect of Gauss's separation method: the structure of the horizontal and vertical components of the field in the separation surface constrain the sum and the difference, respectively, of the interior and exterior potentials' spectral functions. (This same idea is emphasized by Olsen et al. (2010) for the spherical case.) These differing dependencies thus provide two independent equations for two unknown spectral functions, $\tilde{\chi}^\pm$.

The sum and the difference of equations (13) and (17) can then be used to find both the spectral functions, $\tilde{\chi}^\pm$,

$$\tilde{\chi}^\pm(k_x,k_y) = \frac{1}{2}\left(\frac{\mathrm{i}\mathbf{k}_h\cdot\tilde{\mathbf{B}}_h(k_x,k_y)}{k_h^2} \mp \frac{\tilde{B}_z(k_x,k_y)}{k_h}\right)\ , \tag{18}$$

which can then be Fourier transformed to yield $\chi^\pm(x,y,z)$. While we used continuous Fourier transforms, the translation to discrete Fourier transforms is straightforward. Knowledge of $\chi^\pm(x,y,z)$ can then be used to determine $\mathbf{B}^<(x,y,z)$ for $z\geq 0$ and $\mathbf{B}^>(x,y,z)$ for $z\leq 0$, including the part of the photospheric field due to interior currents, $\mathbf{B}^<(x,y,0)$, and the part due to coronal currents, $\mathbf{B}^>(x,y,0)$.

We remark that Welsch & Fisher (2016) found that the potential fields determined separately from Neumann and Dirichlet boundary conditions taken from active-region vector magnetograms were inconsistent with each other. This inconsistency is only problematic if the coronal field is assumed to truly potential; Welsch & Fisher (2016) ascribed the inconsistency between these potential fields to presence of horizontal currents. As shown by Figure 1, antisymmetric horizontal currents above/below the photosphere contribute to the Dirichlet boundary condition at the photosphere (left panel), while symmetric horizontal currents produce the Neumann boundary condition there (middle panel). Gauss's method exploits (i) the inconsistency between these boundary conditions and (ii) the differing asymptotic behaviors of the interior and exterior potential functions to determine which components of the field arose from currents interior to the separation surface, and which arose from currents exterior to it.

2.1. *Other Methods of Solution*

Although we have presented a Fourier method for solving for $\chi^\pm$, other methods can be used to solve Equations (5) and (6). Then the two solutions of these two equations can be used to solve for $\chi^\pm$ individually. For instance, Welsch & Fisher (2016), in their appendices, presented Green's function approaches for each equation.

Several methods of solving Equation (4), a 2D Poisson equation are available. A Fourier approach could be used, with the stream function's 2D Fourier transform, $\tilde{T}(k)$, given by

$$\tilde{T}(k_x, k_y) = \mu_0 \tilde{J}_z(k_x, k_y)/(k_x^2 + k_y^2) \ , \tag{19}$$

where $\tilde{J}_z(k_x, k_y)$ is the 2D Fourier transform of $J_z(x, y, 0)$. For the Fourier methods presented here, IDL routines using discrete Fourier transforms have been posted online,[1] along with brief documentation, a sample input data file, and example results. The Green's function solution for the Cartesian, 2D Poisson presented by Welsch & Fisher (2016) could be used here, too. Kazachenko et al. (2014) employed the FISHPACK software routines (Swarztrauber & Sweet 1975) to solve 2D, Cartesian Poisson equations with either Dirichlet or Neumann conditions on their perimeters. These routines were developed at NCAR, which recently ceased hosting this software online; but they are posted elsewhere.[2]

When solutions T and $\chi^{\pm}$ to equations have been found, if the rotational and irrotational parts of $\mathbf{B}_h$ are sought, these can be computed via

$$\mathbf{B}^{\rm rot} = \nabla_h \times T\,\hat{\mathbf{z}} \ , \text{ and} \tag{20}$$

$$\mathbf{B}^{\rm irrot} = -\nabla_h \chi^+ - \nabla_h \chi^- \ , \tag{21}$$

respectively. We note, though, that

$$\mathbf{B}_h = \mathbf{B}^{\rm rot} + \mathbf{B}^{\rm irrot} \tag{22}$$

will only be satisfied if the observed $\mathbf{B}$ has no mean, horizontal field — if it does, then this mean component must be explicitly added to either $\mathbf{B}^{\rm rot}$ or $\mathbf{B}^{\rm irrot}$, or partitioned between the two. Similarly, if $B_z(x, y, 0)$ has a spatially constant, mean vertical field — that is, a monopole term — then a matching, constant vertical field must be added to $\mathbf{B}^{<}$ or $\mathbf{B}^{>}$, or partitioned between the two.

In Appendix A, we further consider the uniqueness of the rotational / irrotational decomposition. To summarize that discussion: one could add equal and opposite horizontal magnetic fields that are both irrotational and have zero horizontal divergence to $\mathbf{B}^{\rm rot}$ and $\mathbf{B}^{\rm irrot}$, without violating Equations (4) or (5) and still satisfy Equation (22). Doing so would increase the L_2-norms of both $\mathbf{B}^{\rm rot}$ and $\mathbf{B}^{\rm irrot}$ — i.e., this would increase the "2D magnetic energy" in both fields. Thus, the solutions to Poisson's equations, without curl- and horizontal-divergence-free additions yields the "minimum 2D energy" solution.

2.1.1. *Relationship to Potential Toroidal Decomposition*

In spherical geometry, a poloidal-toroidal decomposition (PTD; see, e.g., Chandrasekhar 1961; Backus 1986; Lantz & Fan 1999; Fisher et al. 2010) of the surface magnetic vector field has been employed with Gauss's separation method (e.g., Backus 1986; Olsen et al. 2010; Schuck et al. 2022). To make our presentation understandable in those terms, we digress to briefly relate our development to the Cartesian version of PTD. Because $\mathbf{B}$ is divergence free, it can be expressed in terms of two scalar potential functions, P and T, corresponding to the field's poloidal and toroidal parts, respectively,

$$\mathbf{B} = \nabla \times (\nabla \times P\,\hat{\mathbf{z}}) + \nabla \times (T\,\hat{\mathbf{z}}) \tag{23}$$

$$= \nabla_h(\partial_z P) - \nabla_h^2 P\,\hat{\mathbf{z}} + \nabla_h \times (T\,\hat{\mathbf{z}}) \ . \tag{24}$$

The photospheric field's Cartesian components can be expressed in terms of the PTD potentials as

$$B_x = \partial_x(\partial_z P) + \partial_y T \tag{25}$$

$$B_y = \partial_y(\partial_z P) - \partial_x T \tag{26}$$

$$B_z = -\nabla_h^2 P \ ; \tag{27}$$

the irrotational part of $\mathbf{B}_h$ is given by the $(\partial_z P)$ terms, and the rotational part of $\mathbf{B}_h$ comes from the T terms.

Because all components of $\mathbf{B}$ in equation (23) are derived from curls, the PTD representation of any 3D magnetic field is divergence-free if consistent numerical schemes are used to compute the curls of the potential functions and

[1] http://solartheory.ssl.berkeley.edu/~welsch/public/software/Decomposing_photospheric_B/ – note that underscores and LaTeX's tilde symbol might not copy+paste properly, and should be retyped.

[2] http://solartheory.ssl.berkeley.edu/~fisher/public/software/Fishpack4.1/ – note that LaTeX's tilde symbol might not copy+paste properly, and should be retyped.

divergence of $\mathbf{B}$. From the structure of equation (23), one can see that the vector potential $\mathbf{A}$ whose curl gives $\mathbf{B}$ can be written

$$\mathbf{A} = (\nabla \times P\,\hat{\mathbf{z}}) + T\,\hat{\mathbf{z}} + \nabla\Lambda \ , \tag{28}$$

where we have defined a gauge function Λ.

Equation (27) shows that the poloidal potential P can be found by solving a Poisson equation with source $-B_z(x,y)$. Equation (4) can be derived as the vertical component of the curl of equation (24), with Ampère's law. The horizontal divergence of the horizontal component of equation (24) relates the irrotational part of $\mathbf{B}_h$ to the vertical derivative of the poloidal potential, $\partial_z P$, by yet another Poisson equation,

$$\nabla_h^2(\partial_z P) = (\nabla_h \cdot \mathbf{B}_h) \ . \tag{29}$$

It may be seen that $\nabla_h^2(\partial_z P) = -\partial_z B_z$, implying that the solution to equation (29) is related to the magnetic field's 3D structure above and below the surface imaged by the magnetogram.

Fisher et al. (2010) noted that, for a potential field, with $\mathbf{B} = -\nabla\chi$,

$$\chi(x,y,z) = -\partial_z P^{(\mathrm{P})}(x,y,z) \ , \tag{30}$$

where $\partial_z P^{(\mathrm{P})}$ is the vertical derivative of the poloidal potential for a current-free field (not the observed field), and the potential field's poloidal potential solves the 3D Laplace equation,

$$\nabla^2 P^{(\mathrm{P})} = 0 \ . \tag{31}$$

These last few equations enable translating our development of Gauss's separation in terms of $\chi^{\pm}$ into terms of the PTD potential P and its vertical derivative. In our case, Equations (27) and (29) involve poloidal potentials $P^{\pm}$,

$$-\nabla_h^2 P^+ - \nabla_h^2 P^- = B_z \tag{32}$$

$$\nabla_h^2(\partial_z P^+) + \nabla_h^2(\partial_z P^-) = (\nabla_h \cdot \mathbf{B}_h) \ , \tag{33}$$

where $\nabla^2 P^+ = 0$ holds for $z \le 0$ and $\nabla^2 P^-$ holds for $z \ge 0$. As with our development of Gauss's separation in terms of $\chi^{\pm}$, we have two equations for the two unknown potential functions, $P^{\pm}$.

2.2. *Example:* $\mathbf{B}^{\mathrm{rot}}$, $\mathbf{B}^{<}$, *&* $\mathbf{B}^{>}$ *in AR 10930*

To illustrate results of using the decomposition in Equation (3) with observed magnetic fields, we apply it to the observed photospheric magnetic field of AR 10930. This active region was the focus of a detailed comparison of several NLFFF coronal field models by Schrijver et al. (2008), so several models of its coronal currents have been made. It possessed a strongly sheared central polarity inversion line and produced an X3.4 flare on 2006/12/13, with a peak in GOES soft X-rays at 2:40 UT. The region was relatively near disk center at this time, with the USAF/NOAA Solar Region Summary issued at 24:00 UT on 2006/12/12 reporting its position as S06W21. The magnetogram we have used was prepared for that study, and is available with the electronic version of that paper. It is also posted online.[3] The vector magnetic field was derived from observations by the SpectroPolarimeter (SP; Lites et al. 2013) instrument on the Solar Optical Telescope (SOT; Tsuneta et al. 2008; Suematsu et al. 2008; Ichimoto et al. 2008; Shimizu et al. 2008) aboard the Hinode satellite (Kosugi et al. 2007), using rasters over about 45 minutes starting at 20:30 UT on 2006/12/12. To create the magnetogram used by Schrijver et al. (2008), the SP field was embedded within a larger magnetogram derived from observations of the line-of-sight field made by the Michelson-Doppler Imager (Scherrer et al. 1995). The data were interpolated onto a uniform grid with pixels $0.63''$ on a side, corresponding to 460 km at the solar photosphere. All potentials derived for AR 10930 were computed on (320×320) grids, which were then cropped around the central part of the active region to focus on magnetic structure there.

In the top-left panel of Figure 2, we show the observed photospheric magnetic fields in the central portion of AR 10930. The top-right panel shows the rotational component of this AR's horizontal field, plotted over $J_z(x,y,0)$ in grayscale, The bottom-left panel shows vectors of $\mathbf{B}^{<}(x,y,0)$, with $B_z^{<}(x,y,0)$ in background grayscale (saturated at $\pm$ 1250 G). The bottom-right panel shows $\mathbf{B}^{>}(x,y,0)$, with $B_z^{>}(x,y,0)$ in background grayscale (saturated at $\pm$ 625

[3] http://solartheory.ssl.berkeley.edu/~welsch/public/data/Schrijver_etal_2008_NLFFF_input/

G) and $\mathbf{B}_h^{>}(x, y, 0)$ as hot pink vectors. For the background grayscale in this figure and all others in this paper, black areas correspond to negative quantities, and white areas correspond to positive. In this figure, only every fourth vector is plotted, to reduce clutter.

In the top-left panel, counter-clockwise vorticity at the center of the strong, negative field in the upper-right portion of the frame (a sunspot) indicates a large-scale current flows upward there ($J_z > 0$), and clockwise vorticity in the strong, positive flux region toward lower left of the frame (also a sunspot) implies a large-scale current flows downward ($J_z < 0$) there. The top-right panel shows more intense, smaller-scale currents along the sheared PIL. The factor-of-two

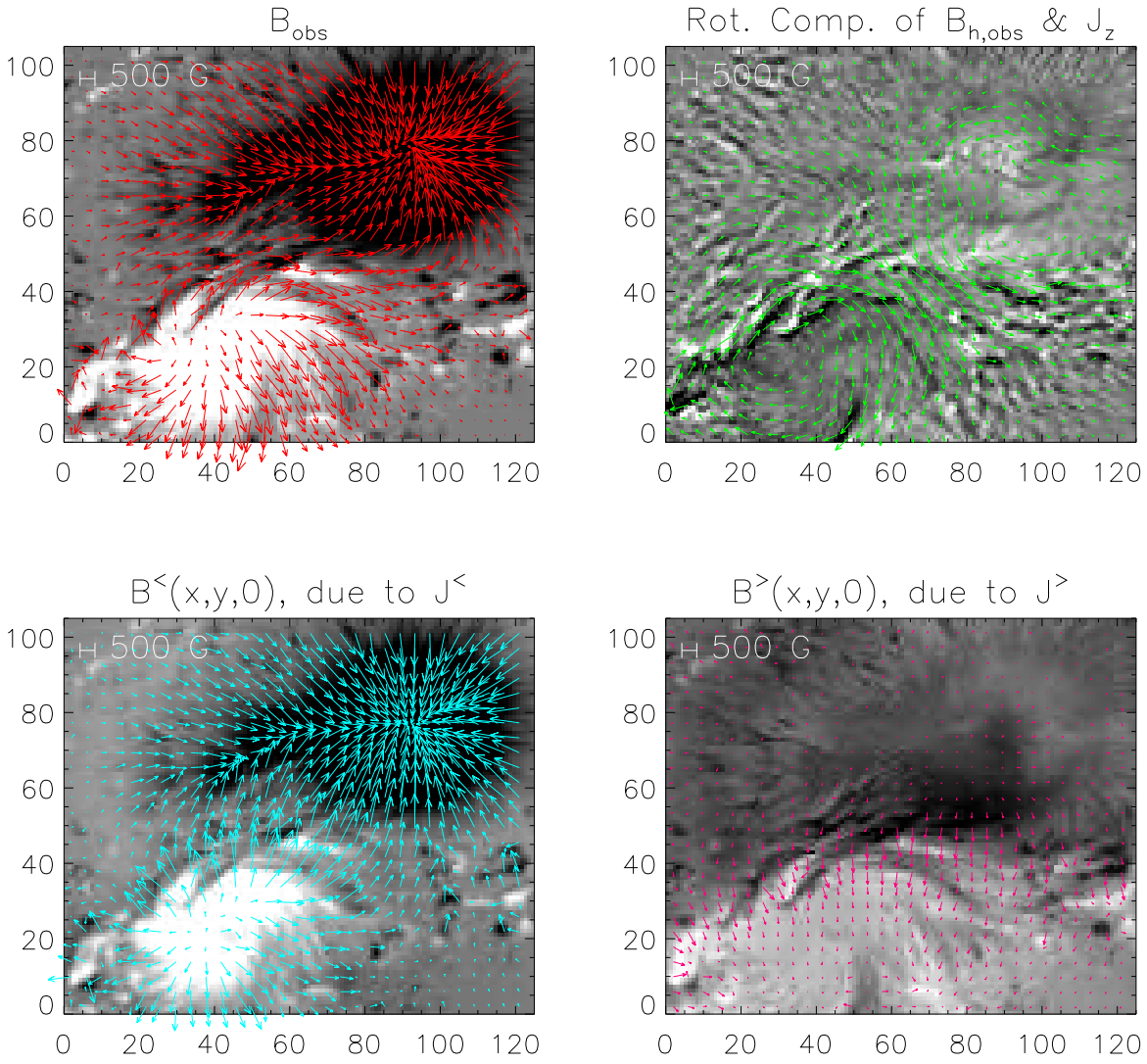

Figure 2. *Top left: The magnetic field in the central region of AR 10930, observed by Hinode/SOT/SP, with rasters starting at 20:30 UT on 2006/12/12. Background grayscale shows B_z, saturated at ± 1250 G. Top right: Vectors show the horizontal field's rotational component, and grayscale shows J_z saturated at ± 50 mA m^{-2}. Bottom-left: Vectors show $\mathbf{B}^{<}(x, y, 0)$, with $B_z^{<}(x, y, 0)$ in background grayscale, saturated at ± 1250 G, and $\mathbf{B}_h^{<}(x, y, 0)$ as aqua vectors. Bottom right: $\mathbf{B}^{>}(x, y, 0)$, with $B_z^{>}(x, y, 0)$ in background grayscale, saturated ± 625 G, and $\mathbf{B}_h^{<}(x, y, 0)$ as hot pink vectors. Only every fourth vector is plotted, to reduce clutter. Horizontal and vertical axes are in units of 0.63″ pixels.*

difference in saturation levels between left and right panels in the bottom row shows that, on average, vertical fields arising from coronal currents are significantly weaker than vertical fields from interior currents. In the bottom-right

panel, an overall dipolar structure in $B_z^>(x, y, 0)$ can be seen, with coronal currents producing negative flux north of the large-scale PIL and positive flux south of it.

Figure 3 shows a larger-scale view of this AR's structure. (The boundary between the SP magnetogram and the larger-field-of-view MDI magnetogram in which it was embedded can be discerned here.) The left-column panels show $B_z^<(x, y, 0)$ (upper) and $B_y^<(x, y, 0)$ (lower) in grayscale, with the saturation set to ± 1250 G in both. The right-column panels show $B_z^>(x, y, 0)$ (upper) and $B_y^>(x, y, 0)$ (lower), but with the saturation set to ± 625 G in both. A rough correspondence between regions having the same sign of B_z can be seen in the top panels. Based on the middle planel of Figure 1, the similarity in $B_z^<$ and $B_z^>$ suggests that substantial parts of the $\mathbf{J}_h^<$ and $\mathbf{J}_h^>$ that produce these fields are symmetric across $z = 0$.

The bottom-left panel shows $B_y^<(x, y, 0)$ in grayscale, with white toward the top of the image. It can be seen that this component of the horizontal field points away from the positive sunspot, and toward the negative sunspot, as would be expected for a potential field. In contrast, the bottom-right panel shows $B_y^>(x, y, 0)$, and this field component points toward page bottom along the main PIL, away from the negative spot and toward the positive spot — i.e., in the "inverse" orientation (Low & Hundhausen 1995; Kuperus & Raadu 1974) with respect to a generic potential field. Very similar near-PIL structure in $\mathbf{B}_h^>$ was observed by Schuck et al. (2022) in AR 12673.

2.2.1. *Statistical Comparisons of* $\mathbf{B}^<$ *vs.* $\mathbf{B}^>$

From the distribution of field strengths in an area of plage in this magnetogram southeast of the positive spot, Welsch (2015) estimated the noise level in the components of $\mathbf{B}$ to be circa 35 G. Among pixels with observed vertical field $|B_z| > 50$ G, the median values of $|B_z^<|$ and $|B_z^>|$ are both about 150 G, but the means of $|B_z^<|$ and $|B_z^>|$ are 360 G and 180 G, respectively. Among this same subset of pixels, the total unsigned flux in $B_z^<$ is 2.7×10^{22} Mx, while in $B_z^>$ the total unsigned flux is 1.4×10^{22} Mx — about half as large. The energies in each of the associated potential fields, that of $\mathbf{B}^<$ in $z \geq 0$ and that of $\mathbf{B}^>$ in $z \leq 0$, are another metric for comparing these fields. The energy of $\mathbf{B}^<$ for $z \geq 0$, $U^{<,\mathrm{pot}}$, can be expressed as a surface integral via

$$2\mu_0 U^{<,\mathrm{pot}} = \int (-\nabla\chi^-) \cdot (-\nabla\chi^-) dV = \int [\nabla \cdot (\chi^- \nabla\chi^-) - \chi^- \nabla^2 \chi^-] dV \tag{34}$$

$$= -\oint (\chi^- \mathbf{B}^<) \cdot \hat{\mathbf{n}}\, dA = \int_{z=0} \chi^- B_z^<\, dA \tag{35}$$

where we apply Equation (7), $\hat{\mathbf{n}}$ is the outward normal from the corona (at the photosphere, it points toward the interior), and only the photosphere contributes to the surface integral because we assume the fields are localized. We note that the potential function χ^- is only determined up to a constant. Requiring that $B_z^<(x, y, 0)$ integrates to zero over the photosphere implies this indeterminacy in χ^- will not affect the integral if a constant were added to χ^-. Using this approach for each field, we find $U^{<,\mathrm{pot}} = 1.1 \times 10^{33}$ erg for $z \geq 0$ and $U^{>,\mathrm{pot}} = 1.8 \times 10^{32}$ erg for $z \leq 0$, so, in this case, the field produced by interior currents contains about six times as much energy as the field from coronal currents. Monte Carlo simulations of changes in these energies due to fluctuations in B_z expected from measurement uncertainties indicate these energies would vary by less than 1%.

2.2.2. *Coronal Currents Implied by* $\mathbf{B}^>$

The morphology of $\mathbf{B}_h^>(x, y, 0)$ and $B_z^>(x, y, 0)$ in Figures 2 and 3 is consistent with a large-scale, coronal current flowing horizontally along and above the AR's large-scale PIL, from the positive-current source in the negative sunspot toward the negative-current sink in the positive sunspot (toward the left and somewhat toward the bottom of the frame). The roughly bipolar character of $B_z^>(x, y, 0)$ near the AR's main PIL is also consistent with this. Given the vorticity evident in the field's rotational component in the upper-right panel of Figure 2, it is plausible that much of this coronal current flows across the photosphere and closes in the solar interior, flowing outward from the negative sunspot and inward at the positive sunspot. (Currents that flow entirely above the photosphere are possible; see, e.g., Longcope 1996.)

Figure 4 shows three arrows, drawn at heights $z > 0$, that illustrate the rough directions of this current, part of the magnetic field that it produces, and part of the potential field. The green arrow is intended to show the approximate direction of a large-scale, volume current in the corona. Such a current would produce a photospheric $\mathbf{B}_h^>(x, y, 0)$ that, as in the observations (small pink vectors), is directed opposite to the blue arrow, which depicts the photospheric potential field's general direction. If a volume current were flowing along the green arrow, then *above* that current, a

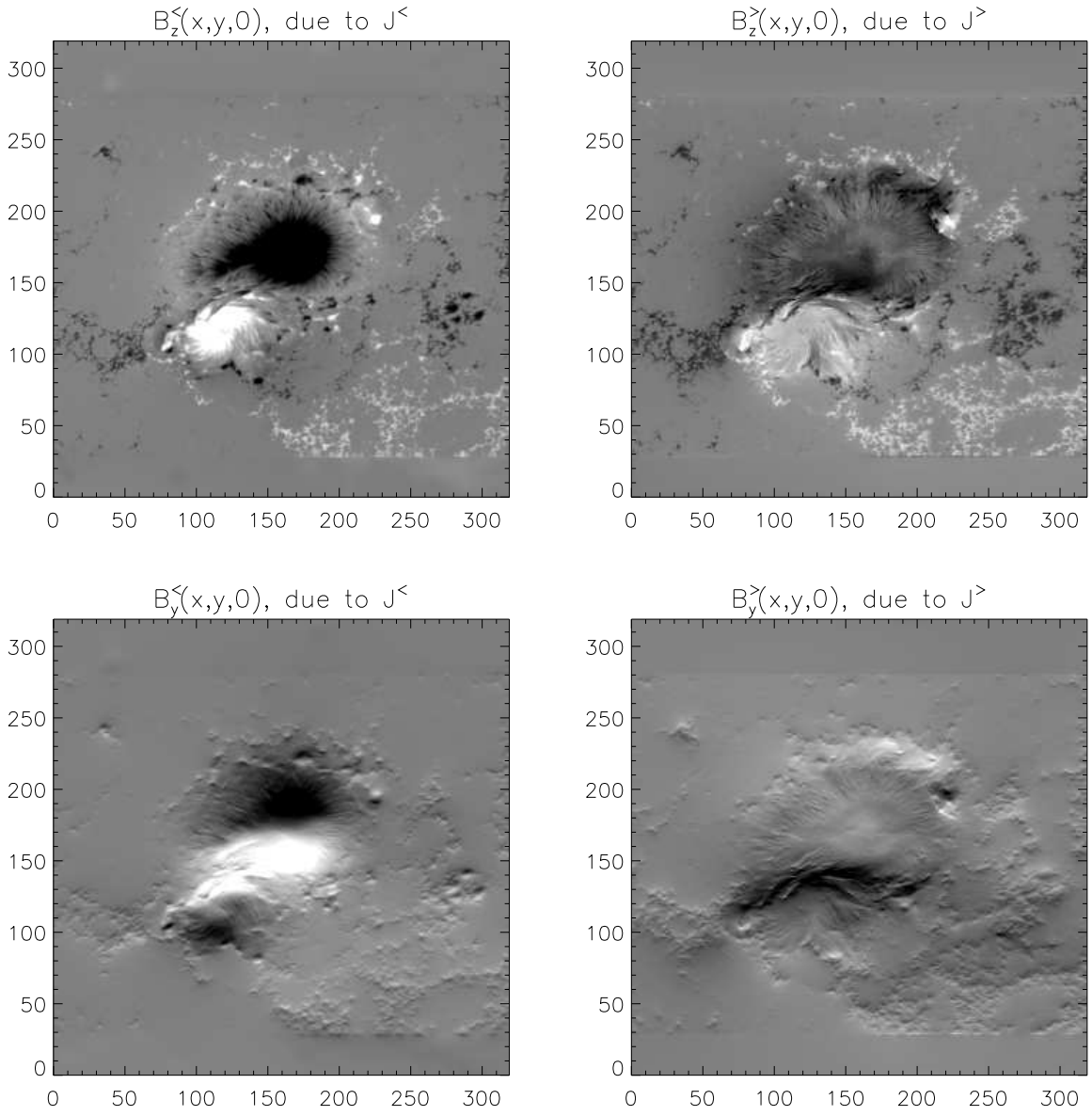

Figure 3. *Left-column panels show $B_z^<(x,y,0)$ (upper) and $B_y^<(x,y,0)$ (lower) from AR 10930 in grayscale, with the saturation set to ± 1250 G in both. The right-column panels show $B_z^>(x,y,0)$ (upper) and $B_y^>(x,y,0)$ (lower), but with the saturation set to ± 625 G in both. For B_y, white (black) is toward the top (bottom) of the page. The white/dark areas in $B_y^<$ in the bottom-left panel are consistent with the horizontal field pointing away from positive-flux regions and toward negative-flux regions. The central dark band in $B_y^>$ in the bottom-right panel is consistent with a coronal current flowing toward the left above that band.*

coronal magnetic field in the direction of pink arrow would be induced, here *along* the potential field's general direction. The presence of the field induced by the volume current higher in the corona is consistent the active region's field being inflated by the excess magnetic energy density (equivalently, excess magnetic pressure) beyond that of the potential field. This inflation of the coronal field will lengthen field lines that arch over the PIL above this large-scale current relative to a field lacking this current. We will revisit the inflation of the coronal field by currents and the implied lengthening of its field lines in Section 5 below.

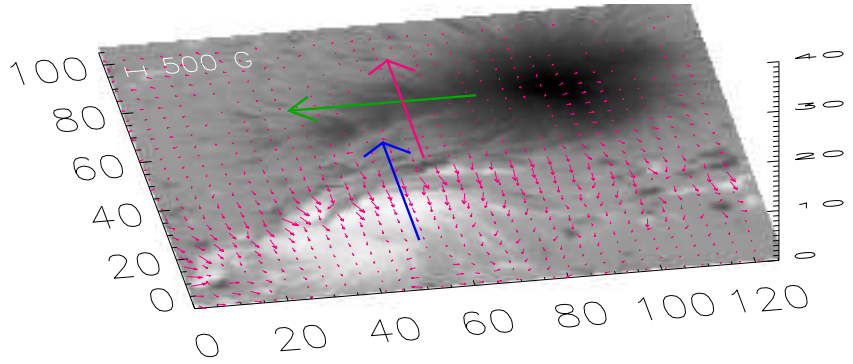

Figure 4. *A perspective view of selected field components in the central portion of AR 10930. Background grayscale shows total photospheric B_z. Small pink vectors show $\mathbf{B}_h^{>}(x,y,0)$, which exhibits a large-scale, coherent pattern along the main polarity inversion line that is consistent with a large-scale, volume current in the corona along the green arrow. Such a current would counter the tendency of the horizontal photospheric field to point in the direction of the potential field (blue). Above the volume current, a field in the direction of the pink arrow (parallel to the large-scale potential field) would be induced. On the $z = 0$ plane, only every fourth vector is plotted, to reduce clutter.*

2.3. *The Potential Coronal Field*

A key step in understanding the structure of currents at and above the photosphere is the comparison of the observed photospheric magnetic field, $\mathbf{B}(x,y,0)$, with the hypothetical, potential magnetic field that would be present if there were no coronal currents. This has typically been done by assuming: (1) that $B_z(x,y,0)$ is determined by currents in the interior, and (2) that coronal currents are rooted in the rotational component of $\mathbf{B}_h(x,y,0)$. One can then solve for a potential χ' whose vertical derivative is consistent with the Neumann condition from $B_z(x,y,0)$.

As we have seen, however, generic coronal currents contribute to $B_z(x,y,0)$; it is only for the special case of antisymmetric currents above and below the photosphere that $\mathbf{J}^{>}$ does not contribute to $B_z(x,y,0)$. Consequently, assuming a current-free corona ($\mathbf{J}^{>} = 0$) would mean that $\mathbf{B}^{>} = 0$, and the coronal field is only $\mathbf{B}^{<}(x,y,z)$. Thus, the appropriate Neumann boundary condition for defining the potential field consistent with a current-free corona is

$$-\partial_z \chi^{-}(x,y,z)|_{z=0} = B_z^{<}(x,y,0) \ , \tag{36}$$

and the horizontal potential field at the photosphere is given by

$$\mathbf{B}_h^{<}(x,y,0) = -\nabla_h \chi^{-}(x,y,0) \ . \tag{37}$$

2.4. *Coronal Free Energy*

Because a potential field satisfying a given Neumann condition is (i) unique and (ii) possesses the minimum possible magnetic energy for that boundary condition (see, e.g., Vekstein 2016), any deviation of the observed field from the potential field indicates the presence of coronal electric currents.

The magnetic energy, U, of the coronal field is given by

$$2\mu_0 U = \int B^2 \, dV \tag{38}$$

$$= \int (\mathbf{B}^< + \mathbf{B}^>)^2 \, dV \tag{39}$$

$$= \underbrace{\int (B^<)^2 \, dV}_{I} + \underbrace{2 \int (\mathbf{B}^< \cdot \mathbf{B}^>) \, dV}_{II} + \underbrace{\int (B^>)^2 \, dV}_{III} \ . \tag{40}$$

We now contemplate how changes in the coronal field during a flare or CME might reduce its magnetic energy. In principle, owing to the high density of the solar interior (relative to the overlying atmosphere), the timescale for fields in the solar interior to respond to changes in the coronal field — mediated by Alfvén waves that communicate news of coronal evolution to fields in the interior — is long (a few hours) relative to the typical flare time scale (a few minutes), so we expect term I above is essentially fixed during a flare / CME. We will test this supposition by comparing pre- and post-flare magnetograms, below.

Because $\mathbf{B}^<$ is potential in the corona, term II can be converted into a surface integral following the approach in Equations (34) and (34),

$$2 \int (\mathbf{B}^< \cdot \mathbf{B}^>) \, dV = 2 \int (-\nabla \chi^< \cdot \mathbf{B}^>) \, dV \tag{41}$$

$$= -2 \int \nabla \cdot (\chi^< \, \mathbf{B}^>) \, dV \tag{42}$$

$$= -2 \oint (\chi^< \, \mathbf{B}^>) \cdot \hat{\mathbf{n}} \, dA \tag{43}$$

$$= 2 \int_{z=0} \chi^< \, B_z^> \, dA \ , \tag{44}$$

where the integral over a closed surface in Equation (43) is replaced by an area integral over the photosphere in Equation (44) because the contribution from the surface at infinity vanishes for localized fields. If one assumes $B_z^>(x, y, 0)$ is zero (e.g., Vekstein 2016), then the integral in Equation (44) vanishes, meaning that term I in Equation (40) would be a lower-bound on the field's energy. As we have seen, however, this assumption is inconsistent with observed photospheric fields. Using Equation (44), term II can be evaluated from data. For the vector magnetic fields of AR 10930 that we have shown in Figure 2, this term is equal to 2.3 $\times 10^{32}$ erg. This is about 20% of the potential energy $U^{<,\mathrm{pot}}$ found above.

Both terms II and III arise from currents above the photosphere, which will, in general, be altered by the magnetic reconnection that is believed to play a central role in flares and CMEs. While term III is always positive if $\mathbf{J}^> \neq 0$, we have not attempted to prove that term II is always positive. In principle, term II might be more negative than term III is positive, implying coronal energy would be *higher* with currents present. As a practical matter, though, because magnetic helicity is approximately conserved even when diffusivity enables reconnection to occur (Berger 1984), the coronal field cannot reach a current-free state.

Based upon these considerations, Schuck (2022, private communication) argues that rather than comparing the energy in a given field, say $\mathbf{B}_1(x, y, z)$, with the energy of a hypothetical current-free state, a more relevant analysis for understanding the energetics of flares and CMEs is probably to compare the energy in $\mathbf{B}_1(x, y, z)$ with that for a different state, $\mathbf{B}_2(x, y, z)$, with altered currents. Nonetheless, following prior convention, we will refer to the difference in energy between a given field, $\mathbf{B}_1(x, y, z)$, and the energy in $\mathbf{B}^<(x, y, z)$ (both for $z \geq 0$) as the free energy in $\mathbf{B}_1(x, y, z)$. In Section 4 below, we consider how changes in coronal currents can release energy.

3. OTHER EXAMPLES OF NON-POTENTIAL PHOTOSPHERIC FIELDS

In this section, we consider the photospheric magnetic field produced by coronal currents, $\mathbf{B}^>(x, y, 0)$, another region, NOAA AR 11158. We then consider a simplistic model of a non-potential, quadrupolar active region. Components of fields in both AR 11158 and the model exhibit properties that are very similar to those of ARs 10930.

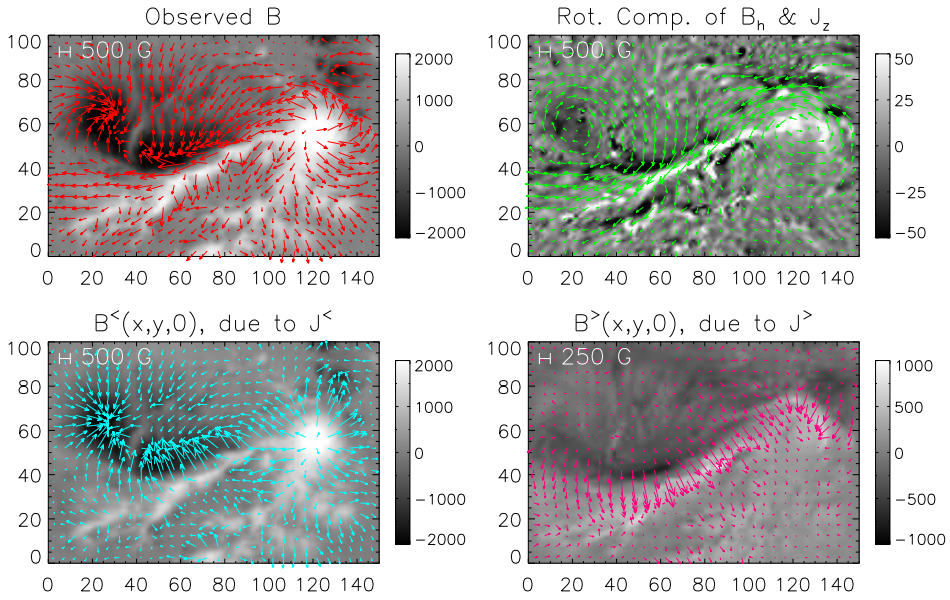

Figure 5. *Top left: the observed horizontal magnetic field in AR 11158, with B_z [G] shown in background grayscale. Top right: Vectors show the horizontal field's rotational component, with J_z [mA m^{-2}] in grayscale. Large-scale upward (downward) currents are present in the positive (negative) flux regions at frame right (left), while smaller-scale, more intense currents are present along the sheared PIL. Bottom left: Vectors of $\mathbf{B}_h^<(x,y,0)$, with $B_z^<(x,y,0)$ [G] in grayscale. Bottom right: Vectors of $\mathbf{B}_h^>(x,y,0)$, with $B_z^>(x,y,0)$ [G] in grayscale. (Note smaller vector scale in this panel.) Both the large-scale, coherent pattern in $\mathbf{B}_h^>(x,y,0)$ along the PIL and $B_z^>(x,y,0)$ are consistent with a large-scale coronal current flowing above the PIL, toward the left and slightly downward (toward the bottom of the frame). In all panels here, only every fifth vector is plotted, to reduce clutter.*

3.1. *Non-Potential Structure in AR 11158*

Like AR 10930, AR 11158 also had a strongly sheared central PIL, and produced an X-class flare, an X2.2 early on 2011/02/15 UT. Notably, this AR appeared to form from the nearby emergence of two separate, large-scale flux tubes (Chintzoglou & Zhang 2013). Chintzoglou et al. (2019) analyzed the development of shear along the central PIL as the nearby footpoints from the two different tubes appeared to collide at the photosphere, which they dubbed collisional shearing.

The first magnetogram of AR 11158 that we will analyze was recorded by the Helioseismic and Magnetic Imager (HMI; Scherrer et al. 2012; Schou et al. 2012 aboard the *Solar Dynamics Observatory* (SDO; Pesnell et al. 2012) near 01:36 UT on 2011/02/15, shortly before the onset (01:44 UT in GOES) of the X2.2 flare. The data were interpolated onto a *plate-caree* grid with pixels 0.5″ on a side, corresponding to 360 km at the solar photosphere. The data preparation procedures used for this magnetogram closely match those employed for the Coronal Global Evolutionary Model (CGEM) project (Hoeksema et al. 2020).

In Figure 5, we show the observed magnetic field (top left), its rotational component $\mathbf{B}_h^{\rm rot}(x,y)$(top right), $\mathbf{B}^<(x,y,0)$ (bottom left), and $\mathbf{B}^>(x,y,0)$ (bottom right). The input data were (895 × 939) arrays, and all intermediate calculations used to create these images were computed on the full input field of view. These were then cropped around two colliding polarities studied by Chintzoglou et al. (2019), which lie in the center of the active region, to enable focusing on magnetic structure there. Only every fifth vector is plotted, to reduce clutter.

The background grayscale of the figure's top-right panel shows $J_z(x,y,0)$. As with AR 10930, we can clearly see that vorticity is present in $\mathbf{B}_h^{\rm rot}(x,y)$, and is associated with the sunspots at either end of this sheared PIL. While the shear in AR 10930 was "internal," due to currents within the single, large-scale flux system that emerged to form that region, shear in this case developed in the collision of the two sunspots shown, along the separatrix (or quasi-separatrix layer; Titov et al. 2002) between two flux systems that emerged, separately, apart from each other at the photosphere. Based on modeling of initially unconnected bipolar fields shearing past each other (e.g., Longcope 1996), the coronal currents generated in this shearing motion need not originate in the interior — they can arise from post-emergence evolution. These considerations suggest that signatures of such currents in photospheric J_z should be small-scale

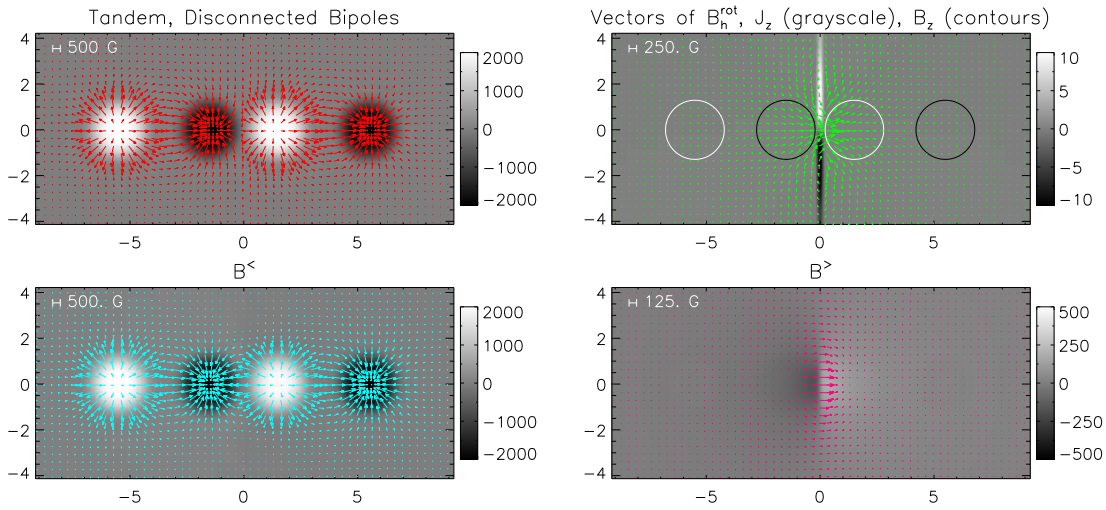

Figure 6. *Top-left: B_z (grayscale, in G) and $\mathbf{B}_h$ (vectors) for a model active region composed of two bipoles that emerged separately, so are disconnected. Fields shown in this and other panels are cropped from a larger domain. For clarity, only every fourth vector is shown. Top-right: vectors show rotational component of $\mathbf{B}_h$ from top-left, grayscale shows J_z [mA m^{-2}], and contours show B_z. Bottom-left: Aqua vectors show $\mathbf{B}_h^<(x, y, 0)$, grayscale shows $B_z^<$ [G]. Bottom-right: Pink vectors show $\mathbf{B}_h^>(x, y, 0)$, grayscale shows $B_z^>$ [G].*

(along separatrices between flux systems), but they should be detectable in the structure of $\mathbf{B}_h^>(x, y, 0)$. We revisit this idea in subsection 3.2 below.

We also note that the evolutionary time scale of coronal currents induced by post-emergence evolution should be shorter than that of current systems that close through through the deep interior (e.g., in large-scale, twisted flux ropes that form ARs), owing to the smaller size of (and therefore smaller self-inductance of) the former. This makes dissipation of post-emergence currents a likely source of much of the energy released in solar flares (and, possibly, small-scale heating events that might drive coronal heating). These ideas have been developed quantitatively by Longcope (1996).

The coherence and direction of $\mathbf{B}_h^>(x, y, 0)$ in AR 11158, as in AR 10930 and AR 12673 (the latter reported by Schuck et al. 2022), suggest that this component of the field arises from a relatively large-scale current flowing in the corona along the PIL, in this case toward the left and slightly down, toward the bottom of the frame.

3.2. *Non-Potential Structure in a Model Active Region*

Proximate emergence of separate flux systems can drive flare activity. In AR 11158, the sheared PIL on which the X2.2 flare occurred ran between photospheric fluxes from large-scale flux tubes that emerged separately (Chintzoglou & Zhang 2013) and then collided (Chintzoglou et al. 2019). When the potential field in cases like this strongly links the two initially disconnected flux systems, their coronal fields can be highly non-potential. Longcope et al. (2005) and Tarr & Longcope (2012) analyzed flare activity in other systems with separate flux emergences. Fu & Welsch (2016) found that emergence of new regions near pre-existing regions was associated with an increase in flaring in the older regions.

We now consider a simple, idealized example of a coronal field that illustrates how non-potential coronal fields are manifested at the photosphere. The configuration is comprised of two untwisted, bipolar flux systems in tandem, and its distribution of B_z — four uniform-field, Gaussian "sunspots" — is shown in the top-left panel of Figure 6. We assume the two bipoles emerged separately. This might be considered a model for separate flux tubes within a single, quadrupolar AR, or two nearby ARs.

Non-potential models based on separately emerging flux systems can be created from potential-field configurations with separatrices by reversing field directions in some homogeneous-connectivity sub-domain(s). To construct the non-potential configuration in Figure 6, we computed the potential field for two co-linear, anti-parallel bipoles, with the photospheric B_z oriented [-++-]; we then reversed all field directions on the left half of the configuration by 180°, so the flipped B_z was [+-+-]. Because the potential field was force-free, the flipped configuration is also force free: all

field lines have the same shape, so their tensions are unchanged; and field strength B is the same everywhere in both cases, so magnetic pressure gradients are unchanged.

In the flipped configuration, however, a current sheet exists on the boundary between the left and right halves of the configuration. Essentially, the induced field from this current system counteracts the potential field's connections between the two systems; see, e.g., Longcope 1996 for a related analysis of currents on separators. Despite the finite width of the J_z channel in the top-right panel of in Figure 6, the actual current distribution is a discontinuity, with the y component of the horizontal field in one constant-x column running opposite those in the adjacent column; the display routine uses interpolation, so smooths sharp image discontinuities. It can be seen that $\mathbf{B}_h^{\rm rot}$ is nonzero even away from $x = 0$, because the gradient of the potential T, the stream function for $\mathbf{B}^{\rm rot}$, is nonzero even where J_z is zero.

As expected, Gauss's analysis reveals the presence of this configuration's coronal non-potentiality from the non-potentiality of its photospheric field: $\mathbf{B}_h^{>}$ and $B_z^{>}$ along the PIL (bottom-right panel) are both consistent with a coronal current flowing toward the bottom of the page. We note that the current in this model does not enter the corona from the emergence of twisted flux tubes from the solar interior — there is no J_z in strong-B_z regions here. Instead, the current is present because the flux systems are disconnected due to their separate emergence. This current here need not close in the interior; rather, the closure current could flow toward the top of the page as a surface current at $z = 0$ (as assumed in the minimum current model of Longcope (1996)). In a solar analog of this model, this closure current would flow in the chromospheric merging layer (or chromospheric canopy), where the field changes from being confined by external plasma pressure at the photosphere and below to being space-filling in the corona.

The fields shown Figure 6 were computed on a grid extending over $\{x, y\} \in [-20, 20]$ units, where 1 unit = 15 Mm, and there are $\simeq 12$ grid points per unit. All fields were then cropped to produce this figure. For clarity, only every fourth vector is shown in each panel.

Despite the sunspots having no twist, this configuration departs strongly from the potential state. The energies of each field can be computed by applying Equation (35). Setting the peak vertical field of each spot to 2000 G and the Gaussian width equal to 15 Mm (1 unit in this figure's panels), this yields an energy for the disconnected field of 12.4 $\times 10^{32}$ erg, and a free energy of 0.7 $\times 10^{32}$ erg, indicating that such a system could produce a significant flare.

4. FLARE-DRIVEN EVOLUTION IN AR 11158

Based on our expectation that coronal currents power solar flares, we expect flare-associated changes in $\mathbf{B}^{>}(x, y, 0)$. These can be compared to changes in $\mathbf{B}^{<}(x, y, 0)$ over the same interval, as we expect that both components will evolve because the flows that drive evolution of solar magnetic fields never cease.

To investigate the nature of changes in AR 11158 in response to the X2.2 flare that began at 01:44 UT on 2011/02/15, we compare the pre-flare magnetic fields described above, observed at 01:36 UT, with the HMI vector magnetic fields measured at 02:12 UT, just after the 02:06 UT end of the flare in GOES soft X-ray observations. We form a relative measure of the fractional change in fields, f, by computing the ratio of the spatially summed absolute *change* in field strength to the summed, absolute, initial field strength,

$$f_i^j \equiv \frac{\sum |\Delta B_i^j|}{\sum |B_i^j|} \ , \tag{45}$$

where $i \in \{h, z\}$ and $j \in \{>, <\}$. We chose to evaluate these sums over the field of view shown in Figure 5, which covers the central part of the area that flared (see, e.g., Figure 5 of Kazachenko et al. 2017). We find $f_h^> = 0.30$ and $f_z^> = 0.24$ for the component of $\mathbf{B}(x, y, 0)$ from coronal currents, and $f_h^< = 0.16$ and $f_z^< = 0.18$ for the component of $\mathbf{B}(x, y, 0)$ from interior currents. Re-computing these f's using the same pre-flare magnetogram and a post-flare magnetogram at 02:36 UT increases the values of the relative changes in both $\mathbf{B}^{>}(x, y, 0)$ and $\mathbf{B}^{<}(x, y, 0)$, with $f_h^> = 0.36$ and $f_z^> = 0.28$ for $\Delta\mathbf{B}^{>}(x, y, 0)$, and $f_h^< = 0.21$ and $f_z^< = 0.23$ for $\Delta\mathbf{B}^{<}(x, y, 0)$. These results suggest that (i) as expected, flare-associated changes are larger in $\mathbf{B}^{>}(x, y, 0)$ compared to $\mathbf{B}^{<}(x, y, 0)$, and (ii) evolution in these field components can cause this measure of relative change to also evolve by a few percent over tens of minutes even outside of GOES flare intervals. We remark that some level of flare-associated changes in $\mathbf{B}^{<}(x, y, 0)$ should not be surprising, because horizontal currents certainly flow in the near-surface interior (where plasma pressure can exert forces on AR magnetic fields), and flare-associated changes in magnetic fields at the photosphere (Wang 1992; Anwar et al. 1993; Kosovichev & Zharkova 1999; Sudol & Harvey 2005; Petrie 2012, 2019) probably extend at least some distance below the photosphere.

To better understand the nature of these changes, Figure 7 shows several aspects of evolution in the fields of AR 11158, by comparing observations at 01:36 UT and 02:12 UT that bracket this flare. The top-left panel shows the observed post-flare $\mathbf{B}^{>}(x, y, 0)$, with $\mathbf{B}_h^{>}(x, y, 0)$ as vectors and $B_z^{>}(x, y, 0)$ in grayscale. A thick yellow contour showing the *pre-flare* PIL of $B_z^{>}(x, y, 0)$ is overplotted here and in other panels, to provide reference points about the structure of the active region. In this panel, blue (red) contours show the post-flare's $B_z^{>}(x, y, 0)$ values of $\{+125, +250\}$ G ($\{-125, -250\}$ G). It may be seen that the PIL in $B_z^{>}$ does not exhibit strong changes. The post-flare structure of $\mathbf{B}_h^{>}(x, y, 0)$, in particular its inverse orientation along the PIL, appears similar to its pre-flare structure (see the bottom-right panel of Figure 5.)

Vectors in the top-right panel show $\Delta\mathbf{B}_h^{>}(x, y, 0)$, the *change* in the horizontal field's coronal component, with the change $\Delta B_z^{>}(x, y, 0)$ in background grayscale (saturated at ± 250 G). Note that bipolar features in grayscale difference images can indicate lateral displacement of structures. Patterns in these field changes are hard to discern, but some changes do exhibit coherence over ~ 20 pixels, or about $10''$ or several Mm.

The Figure's middle row shows changes in the photospheric field's rotational component. Vectors in the middle-left panel show $\Delta\mathbf{B}_h^{\rm rot}(x, y, 0)$, with ΔJ_z, the change in vertical current at the photosphere, in background grayscale. In $\Delta\mathbf{B}_h^{\rm rot}$, several spatially coherent whorl structures in can be seen, also with spatial scales of ~ 20 pixels. In ΔJ_z, several adjacent bipolar structures can be seen, perhaps indicating lateral displacement of some current-carrying structures. Vectors in the middle-right panel also show $\Delta\mathbf{B}_h^{\rm rot}(x, y, 0)$, but with the background grayscale showing the dot product of the unit vector along $\Delta\mathbf{B}_h^{\rm rot}(x, y, 0)$ with the unit vector along the pre-flare $\mathbf{B}_h^{\rm rot}(x, y, 0)$. This shows whether the changes $\Delta\mathbf{B}_h^{\rm rot}(x, y, 0)$ are aligned with or opposite to the pre-flare field's rotational component. While the map of ΔJ_z lacks large-scale structure, the map of dot products reveals spatially coherent behavior: the rotational component in a large neighborhood along the main PIL increased, consistent with the field becoming more horizontal. Some of the whorls in $\Delta\mathbf{B}_h^{\rm rot}(x, y, 0)$ tended to "unwind" the field, such as the whorls with dark backgrounds around pixels with (x, y) coordinates of (10,60) and (110, 60). Some appear to unwind part of the field and wind up another part, such as the bipolar whorls around pixels (30,25) and (50,50).

Vectors in the Figure's bottom row again show changes in the coronal part of the field's irrotational component, $\Delta\mathbf{B}_h^{>}(x, y, 0)$, as in the top-right panel. In the bottom-left panel, though, the background grayscale shows $\Delta(\nabla_h \cdot \mathbf{B}_h)$, the change in the horizontal divergence of the horizontal field, i.e., the change in the source of the field's irrotational component. To the extent that $\mathbf{B}_h^{<}(x, y, 0)$ does changes significantly less in a flare compared to $\mathbf{B}_h^{>}(x, y, 0)$, this should primarily reflect changes in the latter. (Using $\Delta(\nabla_h \cdot \mathbf{B}_h^{>})$ for the background instead does not change the structure in this image substantially.) As with the grayscale map of ΔJ_z in the middle-left panel, however, spatially coherent patterns are not easy to see.

In the bottom-right panel, the grayscale image shows the dot product of the unit vector along $\Delta\mathbf{B}_h^{>}(x, y, 0)$ with the unit vector along the pre-flare $\mathbf{B}_h^{>}(x, y, 0)$. This shows whether the changes $\Delta\mathbf{B}_h^{>}(x, y, 0)$ are aligned with or opposite to the pre-flare horizontal field's coronal component. Structures in this panel exhibit more spatial coherence than structures in the bottom-left panel. Compared to the middle-right panel, however, structures in the bottom-right panel are harder to discern. Over a broad swath along the PIL, though, a tendency for $\Delta\mathbf{B}_h^{>}(x, y, 0)$ to be aligned with the pre-flare $\mathbf{B}_h^{>}(x, y, 0)$ can be discerned.

The increase in the rotational component of the field along the PIL is broadly consistent with reports of fields becoming "more horizontal" due to flares (e.g., Hudson et al. 2008; Wang & Liu 2010; Gosain 2012). This evolution accords with the expectation that the field should contract, or "implode," in a flare (Hudson 2000; Simões et al. 2013; Wang et al. 2018), although when an eruption occurs (as in this case), the ejection's field must open and expand while surrounding, closed (including newly closed, or opened-then-reclosed) fields contract. The persistence in the inverse structure of $\mathbf{B}_h^{>}(x, y, 0)$ along the main PIL suggests that the main coronal current structure remains intact. The intensification of horizontal components of the near-PIL photospheric field is consistent with either an overall decrease in the height at which coronal currents flow or an increase in those currents, or both. If the unwinding areas were at the footpoints of fields that expanded, photospheric twist might decrease (e.g., Barczynski et al. 2020): if the total twist in a segment of a flux tube is fixed, the segment's twist per unit length must decrease if the segment's length increases. Generally, reconnection of a pair of field lines will shorten one and lengthen the other, so observations of such unwinding might be typical. If a flare were not eruptive, though, then the increases in lengths of field lines might be too small for much change in twist per unit length to occur, making such changes difficult to detect.

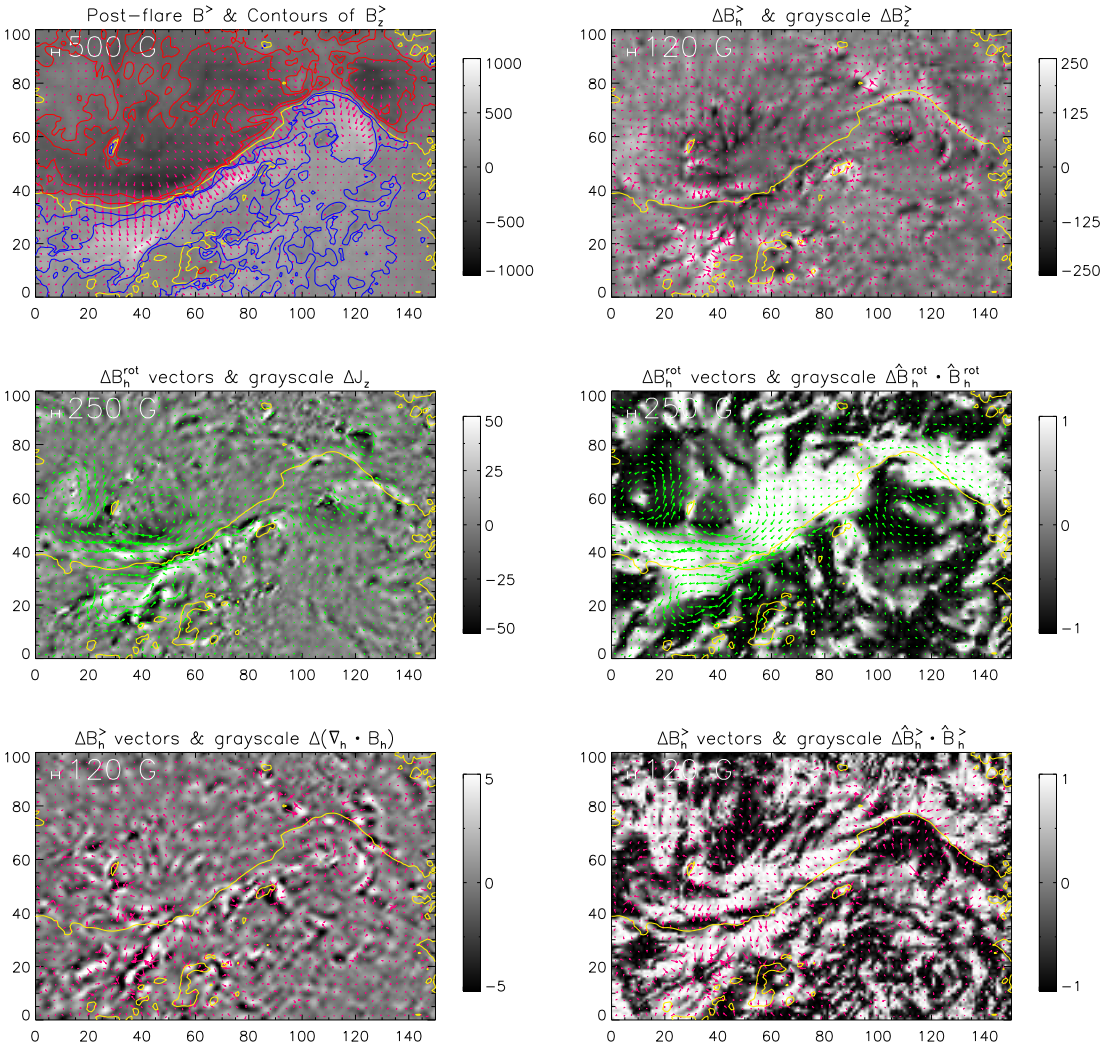

Figure 7. *Top left: the observed, post-flare (02:12 UT) horizontal magnetic field in AR 11158, with B_z [G] shown in background grayscale. Red/blue contours show post-flare values of ±125 G and ±250 G in $B_z^{>}$. A thick yellow contour showing PILs in pre-flare $B_z^{>}$ is also overplotted here and in other panels. Top right: Vectors show $\Delta\mathbf{B}_h^{>}(x,y,0)$ with $\Delta B_z^{>}$ [G] in background grayscale. Middle left: Vectors show $\Delta\mathbf{B}_h^{\rm rot}$, with ΔJ_z [mA m^{-2}] in background grayscale. Middle right: Vectors again show $\Delta\mathbf{B}_h^{\rm rot}$, but the background grayscale shows the dot product of the unit vector along $\Delta\mathbf{B}_h^{\rm rot}$ with the unit vector along the pre-flare $\mathbf{B}_h^{\rm rot}$. Bottom left: Vectors of $\Delta\mathbf{B}_h^{>}$, with $\Delta(\nabla_h \cdot \mathbf{B}_h)$ — the change in the source of the horizontal field's irrotational component — in background grayscale [10^{-6} G cm^{-1}]. Bottom-right: Vectors again show $\Delta\mathbf{B}_h^{>}(x,y,0)$, with grayscale showing the dot product of the unit vector along $\Delta\mathbf{B}_h^{>}$ with the unit vector along the pre-flare $\mathbf{B}_h^{>}$. In middle-right and bottom-right panels, white areas show where changes in vectors are aligned with pre-flare vectors, black areas show changes opposing pre-flare vectors.*

This flare also caused interesting changes in twist in AR 11158's photospheric fields. Recently, Liu et al. (2022) reported flare-related magnetic changes in two measures of twist, both related to what we define as α_z,

$$\alpha_z(x,y) \equiv \frac{[\nabla \times \mathbf{B}(x,y,0)]_z}{B_z(x,y,0)} = \frac{\mu_0 J_z(x,y,0)}{B_z(x,y,0)} \ , \tag{46}$$

where the z subscript reflects that this estimates the α in Equation 1 using only the z component of $\mathbf{J}$. They found that two spatial averages of α_z, one unweighted (which can be large where $|B_z|$ is small) and one weighted by $B_z^2(x,y,0)$, both decreased in areas near flare sites prior to eruptions, then increased after the eruptive flares. As Liu et al. (2022) note, the B_z-weighting de-emphasizes values of twist where $B_z(x,y,0)$ is small, both along at PILs (Tiwari et al. 2009) and in weak-field pixels (Leka & Skumanich 1999). The analysis by Liu et al. (2022) superposed average twists

from many regions, so did not explore the spatial distribution of changes in α_z in individual flares. To illustrate how photospheric twist changed in this flare, Figure 8 shows the structure of $(\alpha_z B_z^2)$ before and after the flare, at 01:36UT and 02:12UT, respectively, as well as maps of the signed and unsigned differences in this quantity. (The GOES flare started at 01:44UT, peaked at 01:56UT, and ended at 02:06UT, so the post-flare map of α_z is close to the flare's end. It is therefore possible that some aspect of flare emission might cause artifacts in HMI's spectral line, which could influence this map. A map of α_z at 02:36UT, however, does not look significantly different.) The top-left and top-right

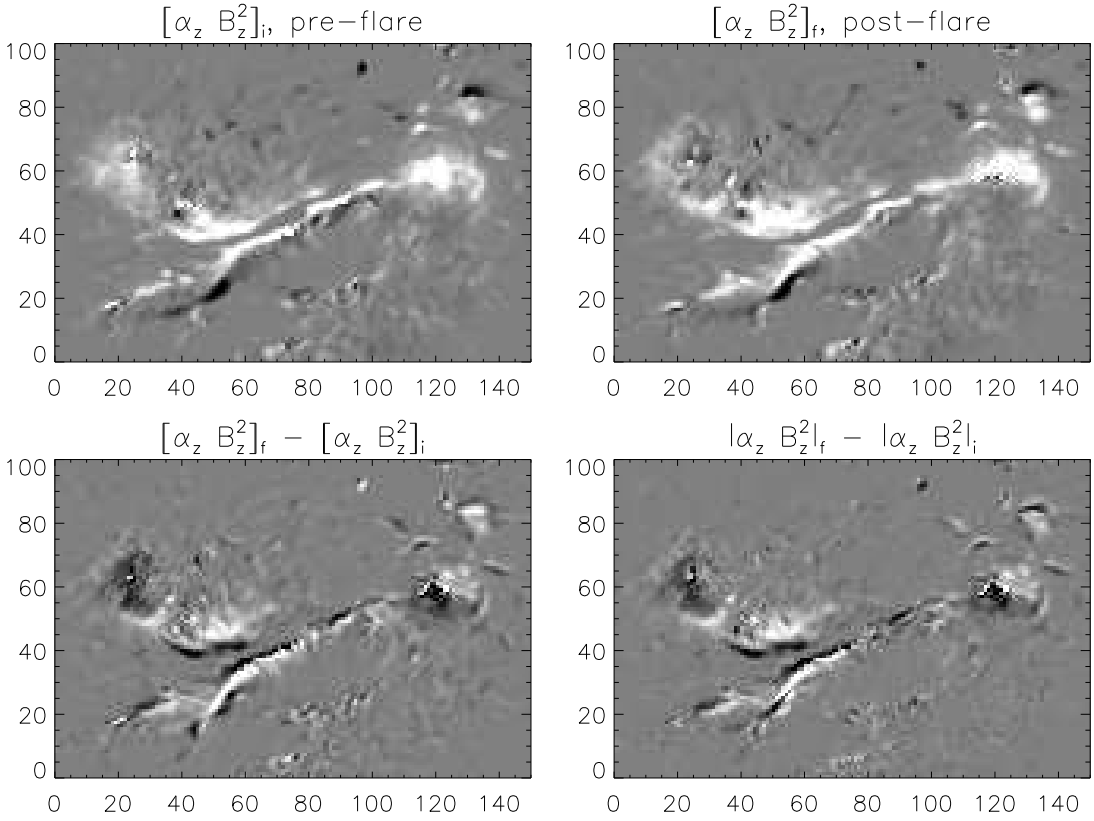

Figure 8. *Top left: pre-flare map of $\alpha_z B_z^2$, at 01:36UT, with white positive and black negative, and saturated at 10^{-2} G^2 cm^{-1}. Top right: post-flare map of $\alpha_z B_z^2$, at 02:12UT. Bottom left: Map of the difference between the upper right array and upper left array. White indicates areas that became more positive, black areas that became less positive. Bottom right: Map of the difference between the absolute values between the upper right array and the upper left array. White indicates areas in which $|\alpha_z B_z^2|$ grew, black indicates areas where this magnitude decreased. Horizontal motion of features produces white where features arrived, and black where they departed. Spread of this measure of twist outward from the PIL can be seen.*

panels show pre- and post-flare distributions of $(\alpha_z B_z^2)$, respectively. The unsigned difference map in the bottom-right panel is bright where $|\alpha_z B_z^2|$ increased, and dark where it decreased. In it, the two unwinding regions discussed above can again be seen near the left and right sides of the frame. Another prominent feature is the evident lateral spread of twist outward from the PIL along its left half: white areas lie farther from the PIL then black, corresponding to motion away from the PIL. The spreading can also be seen in the top panels when comparing the gap between the bright bands that straddle the PIL: the post-flare gap is slightly wider. (A difference map of α_z not weighted by B_z^2 [not shown] is much noisier but shows evolution consistent with the weighted difference image: a dark band runs along the PIL, with two bright bands of straddling the outside the central, dark band.) Outward displacements appear to range from 1 – 3 pixels in extent, or $\sim$ 700 km. The areas of outward spread correspond to areas in which flare ribbons passed, suggesting the changes in α_z are related to the coronal reconnection believed to indirectly produce the ribbons (e.g., Kazachenko et al. 2017). This outward spread in twist might represent spatial diffusion of twist via reconnection between fields of different twist, consistent with magnetic relaxation hypothesized by Taylor (1974) to operate in laboratory plasmas and reported to operate in solar flares by Nandy et al. (2003). Antiochos et al. (2002)

noted that line tying of the coronal field implies that twist could only diffuse within flux systems that reconnect, which is consistent with the observed spread of twist here. Liu et al. (2022) also noted that the changes in twist that they observed were consistent with Taylor's hypothesis.

This observed change in twist could also occur from the decrease in height of a coherent (over ∼30 pixels ∼ 10 Mm), horizontal, mostly-emerged twisted flux rope or similar structure: if this structure were to move down toward the photosphere, the area of its intersection would increase, making it appear that twist had spread laterally. While the eruption of flux ropes has been hypothesized as one mechanism for CMEs, our observations appear to correspond to the *decrease* in height of a flux rope. A partial eruption (Gibson & Fan 2006) could explain both the ejection in this flare and decrease in height of the remaining, twisted fields.

Decreases in the lengths of field lines and/or the currents they carry are consistent with decreases in the inductive energy in the coronal current system. The self-inductance energy, $U^{\rm ind}$, of a thin ribbon of current in the corona scales like that of a wire loop (e.g., Longcope 1996)

$$U^{\rm ind} \propto \mathcal{L} I^2 \propto \Phi I \ , \tag{47}$$

where $\mathcal{L}$ is the current system's self-inductance (which strongly depends on the ribbon's length, L), I is the current it carries, and Φ is the flux enclosed by the current loop, related to $\mathcal{L}$ and I by the definition of self-inductance, $\Phi = \mathcal{L} I$. In general, the magnetic reconnection thought to operate in flares changes fields lines' lengths, alters coronal currents (both their magnitudes and where they flow), and transfers flux between domains of differing connectivity, so $\{L, I, \Phi\}$ could all change. To lower this inductive energy, one or more of these variables must decrease.

The analog of Equation (47) for space-filling currents is

$$U^{\rm ind} = \frac{1}{2} \int \mathbf{J} \cdot \mathbf{A} \, dV \ . \tag{48}$$

In Appendix B, we show that this can be understood in terms of the inductive energies of a set of currents, and that this expression includes both self- and mutual-inductance (Melrose 1997) terms. Thus, the analysis given above for a single, thin ribbon of current (or wire loop) applies more generally: the decrease in coronal energy in flares should arise from *overall* (i) shortening of field lines (recognizing that some can expand — notably so in an eruption), and / or (ii) decreases in coronal currents (recognizing that current density might increase in some areas), and /or (iii) reduction in the fluxes enclosed by currents. We refer to this prediction as the Decrease in Inductive Energy (DIE) hypothesis.

Testing this hypothesis requires further study of the nature of changes in the coronal currents as a result of flares, which, in turn, likely requires either modeling of coronal fields and their flare-associated changes, or better observations of these — only so much can be learned from photospheric field measurements. Here, we consider the use of NLFFF extrapolations to study flare-related changes in coronal fields. Analyzing time series of NLFFF extrapolations around the times of X-class flares, Liu et al. (2022) recently found significant decreases in (i) free magnetic energy in both eruptive and confined flares and (ii) magnetic helicity in eruptive flares. They used an optimization-method code (Wiegelmann 2004) to extrapolate coronal fields.

For testing the DIE hypothesis, however, a Grad-Rubin (G-R) approach (e.g., Grad & Rubin 1958; Wheatland 2007) has several advantages. These methods exploit the fact that coronal fields are anchored at the photosphere, and attempt to match the observed photospheric distributions of $B_z(x, y, 0)$ and $J_z(x, y, 0)$ within a given polarity. The coronal field is evolved based on equation (1), which implies $\mathbf{B} \cdot \nabla \alpha = 0$, i.e., that α must be constant along each field line. At each iteration of the solution process, field lines are traced, and α along each field line is updated to the value $\alpha_{\rm ph}$ at *one* of its footpoints — generally, α will not match both, but attempts to optimize agreement with both have been made (Wheatland & Régnier 2009; Wheatland & Leka 2011; Mastrano et al. 2020). The updated $\mathbf{B}$ is then derived, and this process repeats. Thus, because G-R methods integrate field lines during the solution process, they enable relatively easy characterization of changes in field lines' lengths from before to after a flare. G-R methods that employ vector potentials (e.g., Wheatland (2007)) have another advantage: the coronal flux enclosed by a given field line can be found by integrating the vector potential along that field line, from one footpoint to its conjugate through the model corona, and then back across the model's bottom boundary to the original footpoint, to form a closed loop (see Equation B26). The modeled current on a given field line can be determined from the twist parameter, α, at that field line's footpoint. Thus, a G-R model can readily provide the key pieces of information — the lengths of field lines, the currents they carry, and the coronal fluxes they enclose — to test whether flare-associated changes in

the coronal field obey the DIE hypothesis. In principle, NLFFF models derived from data-driven magnetofrictional simulations, like those in the CGEM model (Hoeksema et al. 2020), could be used to study flare related field changes. As implemented, however, the CGEM model enforces agreement with the observed B_z but not the observed $\mathbf{B}_h$, and so its consistency with observed photospheric vector fields has not been assessed.

5. CONCLUSIONS: SUMMARY, IMPLICATIONS, & FUTURE WORK

5.1. *Photospheric Imprints: Knowns & Unknowns*

In a few flare-producive active regions, Gauss's separation method reveals striking patterns in the photospheric imprints of coronal currents, $\mathbf{B}^{>}(x, y, 0)$. The morphology of large-scale features in $\mathbf{B}^{>}(x, y, 0)$ near PILs strongly suggests that they arise from coherent, relatively large-scale horizontal coronal electric currents flowing above those PILs. In a simple non-potential model of a quadrupolar AR, we find structure in $\mathbf{B}^{>}(x, y, 0)$ similar to that in the observations.

While much research has focused on the structure of B_z and J_z — related to the horizontal curl of the horizontal field — Equation 5 shows that $\nabla_h \cdot \mathbf{B}_h$ contributes to $\mathbf{B}_h^{>}(x, y, 0)$, so reflects aspects of coronal currents. This quantity can differ substantially between fields with similar distributions of B_z and J_z, with the difference being related to currents in the corona. To illustrate this, consider the vector field in two cross sections of a spheromak field (e.g., Rosenbluth & Bussac 1979; Priest & Forbes 2000), as illustrated in Figure 9. Each cut across the spheromak field, at heights $\pm z_0$, may be envisioned as a photospheric boundary condition, with an overlying coronal field. The field above the upper cut, however, differs radically from the field above the lower cut, despite their matching distributions of B_z and J_z: the latter contains a "floating" flux rope. The key characteristic of the photospheric imprint of this coronal flux rope in the lower cut is the inverse orientation (Low & Hundhausen 1995; Kuperus & Raadu 1974) of the horizontal field at the PIL, which points from negative B_z toward positive B_z. The signs $\nabla_h \cdot \mathbf{B}_h$ in the two cuts are opposite, so $\mathbf{B}^{>}(x, y, \pm z_0)$ differs dramatically between the cases.

Much work to understand basic aspects of photospheric imprints in these and other ARs remains to be done. To relate features in imprints to coronal currents, joint analysis of coronal NLFFF models and imprints shows promise. A fundamental step in understanding imprints is identification of the coronal currents that produce them. Using the Biot-Savart law with modeled coronal currents, $\mathbf{J}^{\rm mod}(x, y, z)$, as sources, one can compare the photospheric field produced by the model, $\mathbf{B}^{>,\rm mod}(x, y, 0)$ with the observed $\mathbf{B}^{>}(x, y, 0)$. As a first step, such a comparison is an important test of the model's currents: if substantial disagreements are found, then we have learned something important about shortcomings of the model, and should try to understand the origins of these discrepancies. If model-data agreement is substantial, then the model can be used to characterize the coronal sources of $\mathbf{B}^{>}(x, y, 0)$. We expect smaller-scale, intermittent structures in $\mathbf{B}^{>}(x, y, 0)$ to arise from small-scale currents near the photosphere (because higher-order multipole terms decay rapidly with distance), while larger-scale features in $\mathbf{B}^{>}(x, y, 0)$ probably arise from more coherent coronal structures. The development of photospheric imprints as flux emerges is another important area of study.

5.2. *Flare-Driven Evolution of Photospheric Imprints*

We characterized changes in aspects of $\mathbf{B}^{>}$ and $\mathbf{B}_h^{\rm rot}$ caused by an X2.2 flare in AR 11158. We found intensification of $\mathbf{B}^{>}$ and $\mathbf{B}_h^{\rm rot}$ near the PIL, consistent with earlier reports of the photospheric field becoming more horizontal in flares (e.g., Wang & Liu 2010). We also found areas of unwinding of photospheric fields, consistent with reports by Kazachenko et al. (2015) and Barczynski et al. (2020). In addition, we found that areas of strong α_z appear to spread outward from the flaring PIL, which might accord with the expected spatial diffusion of twist as magnetic fields relax via magnetic reconnection (Taylor 1974; Nandy et al. 2003).

We believe photospheric fields becoming more horizontal is consistent with an overall shortening of current-carrying fields that decreases inductive energy in the field. This DIE hypothesis can be explored with models of coronal fields.

5.3. *Pre-Flare Evolution of Photospheric Imprints*

A question we have not addressed is: Do $\mathbf{B}^{>}$ (or $\mathbf{B}^{<}$, or $\mathbf{B}_h^{\rm rot}$) provide any indication prior to a large flare that a such an event is imminent? This raises a related question: What magnetic changes should be expected in the build-up to a flare?

Based upon models (Hudson 2000) and observations (e.g., Simões et al. 2013) finding that coronal fields implode (or deflate, in an overall sense) during flares, we expect that might they *inflate* prior to flares. This might be observable

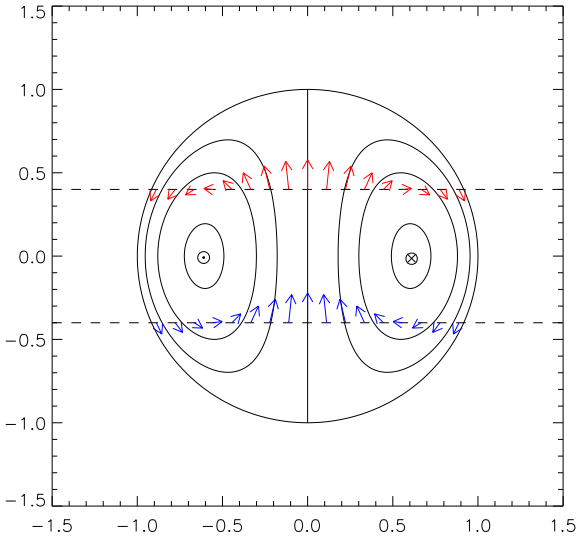

Figure 9. *Solid contours show poloidal field lines from a spheromak field. The dashed lines show two cross sections at* $\pm z_0$*, and vectors show the field on each cross section. The field within the spheromak is a constant-*α*, force-free field. Azimuthal current flows out of the left half of the image, denoted by* $\odot$ *there, and into the right half of the page, denoted by* $\otimes$ *there. Each cross section be envisioned as a photospheric boundary condition, with an overlying coronal field. The field above the upper cut, however, differs radically from the field above the lower cut, despite their matching distributions of* B_z *and* J_z*: the latter contains a "floating" flux rope. The key photospheric imprint of this coronal flux rope in the lower cut is the "inverse" orientation of the horizontal field on its PIL. The horizontal divergence,* $\nabla_h \cdot \mathbf{B}_h$*, in the lower-cut field is opposite to that in the upper-cut field. Consequently,* $\mathbf{B}^{>}$ *differs on the upper and lower cuts.*

as a tendency for coronal fields to slowly expand upward or outward prior to flares. We refer to the predicted upward motion of some parts of pre-flare fields as the Coronal Inflation (CI) hypothesis. Such motion might be related to slow rising motions seen before some eruptions (e.g., Schuck et al. 2004; Sterling & Moore 2005; Liu et al. 2012), but might also be much more subtle (or start earlier) than such slow-rise motions. The disparity in time scales between the slow build-up phase prior to flares and the impulsive release of energy in flares might explain why implosion/deflation has been observed, but inflation has not. Coronal changes during flares are localized and rapid, therefore relatively easy to notice and characterize. In contrast, changes prior to flares are steady and ubiquitous: all parts of the coronal and photospheric magnetic fields are steadily evolving, all of the time. Nonetheless, a clear, testable prediction of the CI model is that fields arching over pre-flare PILs should expand. This hypothesis could be tested by characterizing the evolution of lengths of near-PIL field lines in non-potential models of pre-flare coronal fields (e.g., NLFFF extrapolations).

As shown in Figure 10, some aspects of pre-flare evolution of α_z in AR 11158 appear consistent with coronal inflation. The top-left panel shows a map of $(\alpha_z B_z^2)$ from a bit more than four hours before the flare's onset, and the top-right panel shows a map of $(\alpha_z B_z^2)$ a few minutes before the flare. It can be seen that the gap along the PIL narrows during this interval. As with Figure 8, the unsigned difference map in the bottom-right panel is bright where $|\alpha_z B_z^2|$ increased, and dark where it decreased. The white band near the PIL's bottom edge, and adjacent black band farther from the PIL, suggest that twist moved *toward* the PIL in the hours before the flare. This evolution is the reverse of that observed in Figure 8.

We consider two physical mechanisms, both consistent with the coronal inflation hypothesis, that could explain this pre-flare evolution. First, if flux cancellation (e.g., Amari et al. 2010) occurs along the PIL, the area occupied by sheared, near-PIL fields could shrink. The coronal field can be inflated by flux cancellation (e.g., Forbes & Isenberg 1991) as photospheric reconnection at the PIL untethers current-carrying coronal fields. Second, if an emerging, horizontal flux tube along the PIL were more than half-emerged, then further emergence would decrease the area over

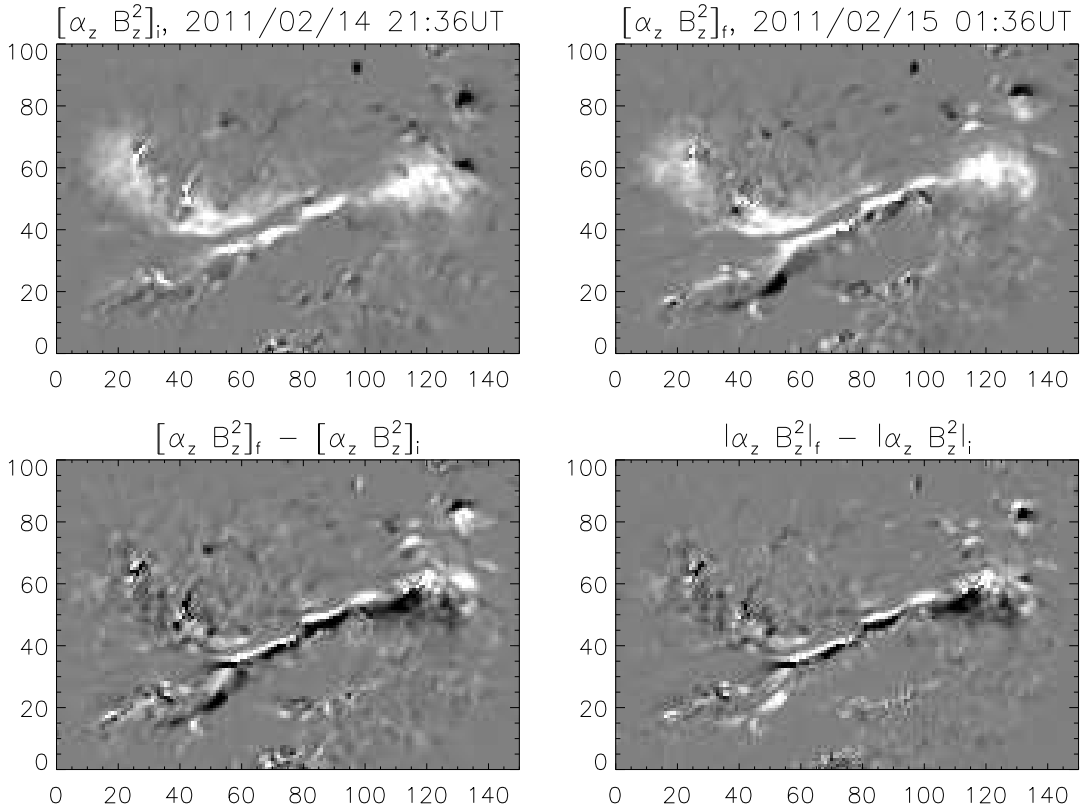

Figure 10. *Top left: map of $\alpha_z B_z^2$, at 21:36UT, four hours before the flare, with white positive and black negative, and saturated at 10^{-2} G^2 cm^{-1}. Top right: pre-flare map of $\alpha_z B_z^2$, at 01:36UT. Bottom left: Map of the difference between the upper right array and upper left array. White indicates areas that became more positive, black areas that became less positive. Bottom right: Map of the difference in absolute values between the upper right array and the upper left array. White indicates areas in which $|\alpha_z B_z^2|$ grew, black indicates areas where this magnitude decreased. Horizontal motion of features produces white where features arrived, and black where they departed. The white band near the PIL and black band farther from the PIL suggest* inward *motion of twist* toward *from the PIL in the hours before the flare. In the top panels, the width of the PIL can be seen to narrow slightly over the same interval. This narrowing might arise from flux cancellation or the further emergence of a mostly-emerged, horizontal flux rope.*

which the flux tube intersects the photosphere, leading to an apparent contraction of the high-twist area. The core of this latter idea was suggested by G. Valori (2022, private communication). Both mechanisms might also explain the pre-flare decreases in α_z reported by Liu et al. (2022).

We note that Gauss's separation method might be able to distinguish which is at work. If a current-carrying flux tube were emerging, then $\mathbf{B}^{<}(x, y, 0)$ might decrease as sub-photospheric currents across the photosphere, with a corresponding increase in $\mathbf{B}^{>}(x, y, 0)$. Alternatively, cancellation at the photosphere could remove high-twist (high-J_z) photospheric flux, and lead to increases in both $\mathbf{B}^{<}(x, y, 0)$ and $\mathbf{B}^{>}(x, y, 0)$ as current-carrying, post-cancellation fields move downward and upward, respectively, from the cancellation site.

We plan to further examine pre-flare changes in α_z for this event, to see if other coherent patterns in its evolution can be identified. And are pre-flare changes in α_z in other events similar to what we find here for AR 11158? To address this question, we also plan to conduct studies of pre-flare magnetic evolution for additional events in other ARs.

5.4. *Future Work*

We now briefly discuss a few areas for further studies of $\mathbf{B}^{>}(x, y, 0)$ motivtaed by the observational and modeling results presented above.

Methods to incorporate information about coronal currents inferred from $\mathbf{B}^{>}(x, y, 0)$ into coronal field extrapolations should be investigated. Because the observed photospheric field contains substantial uncertainties and is not force-

free, observed values of $\mathbf{B}(x, y, 0)$ could be adjusted slightly to improve agreement between modeled and observed $\mathbf{B}^{>}(x, y, 0)$.

Observational studies of differences in active regions' $\mathbf{B}^{>}(x, y, 0)$ — their morphologies and evolution — should be investigated, along with relationships between $\mathbf{B}^{>}(x, y, 0)$ and flare / CME productivity. It is known that ARs with simple bipolar structure are less flare-productive than more complex ARs (e.g., Sammis et al. 2000). Does the structure of $\mathbf{B}^{>}(x, y, 0)$ tend to be simpler in less flare-productive regions?

We have characterized flare-associated changes in $\mathbf{B}_h^{\rm rot}(x, y)$, $\mathbf{B}^{>}(x, y, 0)$, and $\alpha_z(x, y)$ in AR 11158. Such changes should also be investigated in other ARs, to both identify similarities and characterize the degree of variability between ARs. We did not describe changes in $\mathbf{B}^{<}(x, y, 0)$ in detail here, but changes in this quantity should also be studied. Might decreases in $\mathbf{B}^{<}(x, y, 0)$ be used to determine when emerging currents have passed from the interior into the corona?

ACKNOWLEDGMENTS

Acknowledgments: We thank the US taxpayers for providing the funding that made this research possible, and gratefully acknowledge support from NASA LWS 80NSSC19K0072, from NASA and NSF through their funding of the Coronal Global Evolutionary Model (CGEM) project (http://cgem.ssl.berkeley.edu/) to UC Berkeley through NSF award AGS1321474 and through NASA's one-year extension project, "ECGEM," through award 80NSSC19K0622. NASA's SDO satellite and the HMI instrument were joint efforts by many teams and individuals, whose efforts to produce the HMI magnetograms that we analyzed here are greatly appreciated. Hinode is a Japanese mission developed and launched by ISAS/JAXA, collaborating with NAOJ as a domestic partner, and NASA and STFC (UK) as international partners. Scientific operation of the Hinode mission is conducted by the Hinode science team organized at ISAS/JAXA. This team mainly consists of scientists from institutes in the partner countries. Support for the post-launch operation is provided by JAXA and NAOJ (Japan), STFC (UK), NASA (USA), ESA, and NSC (Norway). Last but not least, BTW acknowledges generous support from the Fundación Jesús Serra, which supported a visit to the IAC-Tenerife during which a portion of this work was completed.

APPENDIX

A. MINIMIZING THE L_2-NORM IN ROTATIONAL & IRROTATIONAL PARTS OF $\mathbf{B}$

In this Appendix, we show that, while the decomposition of $\mathbf{B}_h(x, y, 0)$ into rotational and irrotational components on a finite, Cartesian domain is not unique, the solutions we have given in Equations (20) and (21) separately minimize the L_2-norms of $\mathbf{B}_h^{\rm rot}(x, y, 0)$ and $\mathbf{B}_h^{\rm irrot}(x, y, 0)$. Non-uniqueness is not specific to our development of this decomposition, but is an issue for any solution to 2D Poisson equations on finite Cartesian (or less-than-4π spherical) domains: harmonic functions, which are solutions to the 2D Laplace equation (the homogeneous form of the 2D Poisson equation) can always be added to a given Poisson solution and still obey the Poisson equation.

In our case, one could add harmonic functions $T_0(x, y)$ and $\chi_0(x, y)$ to the potentials T and $\chi^{\pm}|_{z=0}$, which solve the 2D Poisson Equations (4) or (5), with

$$T_1 = T + T_0 \ , \tag{A1}$$
$$\chi_1 = \chi^{+}(x, y, 0) + \chi^{-}(x, y, 0) + \chi_0 \ , \tag{A2}$$

where T_0 and χ_0 solve the 2D Laplace equations,

$$\nabla_h^2 T_0 = 0 \tag{A3}$$
$$\nabla_h^2 \chi_0 = 0 \ . \tag{A4}$$

Adding arbitrary harmonic functions T_0 and χ_0 would change the rotational and irrotational horizontal fields by

$$\delta\mathbf{B}_h^{\rm rot} = \nabla_h \times T_0 \, \hat{\mathbf{z}} \tag{A5}$$
$$\delta\mathbf{B}_h^{\rm irrot} = -\nabla_h \chi_0 \ . \tag{A6}$$

Equations (A3) and (A4) imply that $\delta\mathbf{B}_h^{\rm rot}$ and $\delta\mathbf{B}_h^{\rm irrot}$ are each irrotational and divergence-free. But we have extra constraints on T_0 and χ_0, because we demand $\delta\mathbf{B}_h^{\rm rot} - \delta\mathbf{B}_h^{\rm irrot} = 0$, so the sum of $\mathbf{B}_h^{\rm rot}$ and $\mathbf{B}_h^{\rm irrot}$ match the observed $\mathbf{B}_h$ (to within a constant). As Fisher et al. (2010) noted, this implies these harmonic functions satisfy the homogeneous Cauchy-Riemann equations,

$$\partial_x(\chi_0) = -\partial_y T_0 \tag{A7}$$
$$\partial_y(\chi_0) = \partial_x \tilde{T}_0 \ . \tag{A8}$$

Having explained the nature of the non-uniqueness, we next show that setting $T_0 = 0$ minimizes the L_2 norm of the rotational part of $\mathbf{B}_h$,

$$||\mathbf{B}_h^{\rm rot}||_2^2 \equiv \int_S |\mathbf{B}_h^{\rm rot}|^2 dS \ , \tag{A9}$$

and setting $\chi_0 = 0$ minimizes L_2 norm of the irrotational part of $\mathbf{B}_h$,

$$||\mathbf{B}_h^{\rm irrot}||_2^2 \equiv \int_S |\mathbf{B}_h^{\rm irrot}|^2 dS \ . \tag{A10}$$

A.1. *Minimizing L_2 for $\mathbf{B}_h^{\rm rot}$*

To establish the first result, we expand Equation (A9) with $T_0 \neq 0$,

$$\begin{aligned}||\mathbf{B}_h^{\rm rot}||_2^2 = &\int_S |\nabla_h \times T\,\hat{\mathbf{z}}|^2 dS + \int_S |\nabla_h \times T_0\,\hat{\mathbf{z}}|^2 dS + \\ &2\int_S (\nabla_h \times T_0\,\hat{\mathbf{z}}) \cdot (\nabla_h \times T\,\hat{\mathbf{z}}) dS \ . \end{aligned}\tag{A11}$$

We note that

$$\begin{aligned}(\nabla_h \times T\,\hat{\mathbf{z}}) \cdot (\nabla_h \times T\,\hat{\mathbf{z}}) &= (\nabla_h T \times \hat{\mathbf{z}}) \cdot (\nabla_h T \times \hat{\mathbf{z}}) \\ &= (\nabla_h T \cdot \nabla_h T)(\hat{\mathbf{z}} \cdot \hat{\mathbf{z}}) \quad \text{(A12)} \\ &= |\nabla_h T|^2 \ , \quad \text{(A13)}\end{aligned}$$

and similarly for the $|\nabla_h \times T_0\,\hat{\mathbf{z}}|^2$ term.

For both this case and the minimization of L_2 for $\mathbf{B}_h^{\rm irrot}$ (below), our analysis follows the basic approach of Yeates (2017): for the cross-term that results from taking the square of the summed fields, we use a vector identity to create two terms, one of which has ∇_h^2 acting on the solution of the 2D Laplace's equation (either T_0 or χ_0) such that it vanishes, with the other term being converted from an integral over S to a line integral around its boundary ∂S, via the fundamental theorem of calculus (FTOC). For periodic domains, this term vanishes. For non-periodic, localized magnetic fields, the boundary term can be made arbitrarily small if the domain is expanded sufficiently. In such cases, minimizing each norm requires setting T_0 and χ_0, respectively, to zero in each case.

We employ the vector identity $\nabla \cdot (\mathbf{u} \times \mathbf{v}) = \mathbf{v} \cdot \nabla \times \mathbf{u} - \mathbf{u} \cdot \nabla \times \mathbf{v}$, which, with $\mathbf{u} = T\,\hat{\mathbf{z}}$ and $\mathbf{v} = \nabla_h \times \tilde{T}\,\hat{\mathbf{z}}$, becomes

$$\nabla_h \cdot (\mathbf{u} \times \mathbf{v}) = \mathbf{v} \cdot \nabla_h \times \mathbf{u} - \mathbf{u} \cdot \nabla_h \times \mathbf{v} \ . \tag{A14}$$

This means

$$\begin{aligned}(\nabla_h \times T_0\,\hat{\mathbf{z}}) \cdot (\nabla_h \times T\,\hat{\mathbf{z}}) &= \nabla_h \cdot (T\,\hat{\mathbf{z}} \times (\nabla_h \times T_0\,\hat{\mathbf{z}})) \\ &\quad + T\,\hat{\mathbf{z}} \cdot (\nabla_h^2 T_0)\,\hat{\mathbf{z}} \quad \text{(A15)} \\ &= \nabla_h \cdot (T\,\hat{\mathbf{z}} \times (\nabla_h \times T_0\,\hat{\mathbf{z}})) \\ &= \nabla_h \cdot (T\,\hat{\mathbf{z}} \times (\nabla_h T_0 \times \hat{\mathbf{z}})) \\ &= \nabla_h \cdot (T\,\nabla_h T_0) \ , \quad \text{(A16)}\end{aligned}$$

where we also used $\nabla_h \times (\nabla_h \times T_0\,\hat{\mathbf{z}}) = -\nabla_h^2 T_0\,\hat{\mathbf{z}}$, Equation (A3), and the vector identity $\mathbf{u} \times (\mathbf{v} \times \hat{\mathbf{z}}) = \mathbf{v}(\mathbf{v} \cdot \hat{\mathbf{z}}) - \hat{\mathbf{z}}(\mathbf{v} \cdot \mathbf{u})$. Applying the 2D divergence theorem (derived from the FTOC) to the integral of the remaining term, we are left with

$$\begin{aligned}||\mathbf{B}_h^{\rm rot}||_2^2 = &\int_S |\nabla_h T|^2 dS + \int_S |\nabla_h T_0|^2 dS + \\ &2\oint_{\partial S} T(\nabla_h T_0) \cdot \hat{\mathbf{n}}\, d\boldsymbol{\ell} \ , \end{aligned}\tag{A17}$$

where $\hat{\mathbf{n}}$ is the outward unit normal along the boundary of S.

On a periodic domain, boundary term vanishes. On an infinite domain, T goes to zero at infinity, as we now explain. Potentials for a point source on an infinite domain, equivalent to the fundamental solution of the 2D, Cartesian Laplace operator, vary as the logarithm of distance, r, from the source (e.g., Bishop 1996; Welsch & Fisher 2016). The sources of our potentials are, however, dipolar: AR fields should contain no whole-AR imbalance between positive and negative J_z; and $\int (\nabla_h \cdot \mathbf{B}_h) dA = \oint \mathbf{B}_h \cdot \hat{\mathbf{n}}\, d\boldsymbol{\ell}$ must vanish far from a localized active region with no monopole. This means T and $\chi^{\pm}|_{z=0}$ should scale as $\ln(r) - \ln(r+d)$, where d is a characteristic separation between opposite-sign sources. For large r, this implies $T \sim \ln(1 + d/r) \sim d/r$, i.e., $T \propto 1/r$. Similar arguments apply for $\chi^{\pm}|_{z=0}$. Thus, for an infinite domain, T and $\chi^{\pm}|_{z=0}$ go to zero; for the boundary term in Equation (A17) to be finite, the potential would have to diverge.

Minimization of the L_2 norm therefore requires setting T_0 to zero.

A.2. *Minimizing L_2 for $\mathbf{B}_h^{\rm irrot}$*

Turning our attention to χ_0, we expand the square of the L_2-norm in Equation (A10) with non-zero χ_0,

$$\begin{aligned}||\mathbf{B}_h^{\rm irrot}||_2^2 = &\int_S |\nabla_h(\chi^+ + \chi^-)|^2 dS + \int_S |\nabla_h \chi_0|^2 dS + \\ &2\int_S (\nabla_h \chi_0) \cdot \nabla_h(\chi^+ + \chi^-)\, dS \ . \end{aligned}\tag{A18}$$

We first consider the vector identity $\nabla \cdot (u\mathbf{v}) = u\nabla \cdot \mathbf{v} + \mathbf{v} \cdot \nabla u$, which, with $u = (\chi^+ + \chi^-)$ and $\mathbf{v} = \nabla_h \chi_0$, implies

$$\begin{aligned}\nabla_h \chi_0 \cdot \nabla_h(\chi^+ + \chi^-) &= \nabla_h \cdot ((\chi^+ + \chi^-)\ \nabla_h \chi_0) \\ &\quad - (\chi^+ + \chi^-)(\nabla_h^2 \chi_0)) \quad \text{(A19)} \\ &= \nabla_h \cdot ((\chi^+ + \chi^-)\ \nabla_h \chi_0) \quad \text{(A20)}\end{aligned}$$

where we also used equation (A4).

Again applying the divergence theorem to the remaining term, we are left with

$$||\mathbf{B}_h^{\rm irrot}||_2^2 = \int_S |\nabla_h(\chi^+ + \chi^-)|^2 dS + \int_S |\nabla_h \chi_0|^2 dS + 2\oint_{\partial S} (\chi^+ + \chi^-)\ \nabla_h \chi_0 \cdot \hat{\mathbf{n}}\, dL\ . \quad \text{(A21)}$$

Again, for periodic domains, this boundary term vanishes, and for an infinite domain with localized AR fields, the magnitude of $(\chi^+ + \chi^-)$ will decrease with distance from sources in the AR as $1/r$, so the boundary term must vanish if the potential χ_0 does not diverge.

Minimization of the L_2 norm therefore requires setting χ_0 to zero. Yeates (2017) presented a sparse method to find the most spatially compact solution to the 2D Poisson equation, by minimizing the L_1-norm. Those L_1-minimizing solutions do not, in general, minimize the L_2-norm.

B. MAGNETIC ENERGY AS SELF- AND MUTUAL INDUCTIVE ENERGIES

If we envision current-carrying regions of the coronal magnetic field as comprised of a set of discrete currents flowing in very small (even infinitesimal) channels, Equation (48) can be shown to have the same dependence on field lines' length scales, currents, and enclosed fluxes as Equation (47). We first derive Equation (48) from

$$U = \frac{1}{2\mu_0}\int \mathbf{B}\cdot\mathbf{B}\, dV\ , \quad \text{(B22)}$$

to note the explicit role of a boundary term when a the integrals involved do not run over all space. We do so by "uncurling" one factor of $\mathbf{B}$ and moving the curl operator onto the other, with the vector identity $(\nabla\times\mathbf{A})\cdot\mathbf{B} = \mathbf{A}\cdot(\nabla\times\mathbf{B}) + \nabla\cdot(\mathbf{A}\times\mathbf{B})$, yielding

$$U = \frac{1}{2\mu_0}\int \mathbf{A}\cdot(\nabla\times\mathbf{B})\, dV + \frac{1}{2\mu_0}\int \nabla\cdot(\mathbf{A}\times\mathbf{B})\, dV \quad \text{(B23)}$$

$$= \frac{1}{2}\int \mathbf{A}\cdot\mathbf{J}\, dV + \frac{1}{2\mu_0}\int (\mathbf{A}\times\mathbf{B})\cdot\hat{\mathbf{n}}\, dA\ . \quad \text{(B24)}$$

We first consider the case in which the volume under consideration is infinite, but the sources of $\mathbf{B}$ are finite. In this case, $\mathbf{B}$ in the surface term vanishes, so we need only consider the volume term. Conservation of charge implies $\nabla\cdot\mathbf{J} = 0$, so "current lines" of $\mathbf{J}$ form closed loops, just like field lines of $\mathbf{B}$. (If the magnetic field were force-free, $\mathbf{J}$ would be along $\mathbf{B}$, and each current line would correspond to a magnetic field line, but we do not assume $\mathbf{J}\times\mathbf{B} = 0$ here.) We can write $dV = dA_\perp |d\boldsymbol{\ell}|$, where $d\boldsymbol{\ell}$ points along $\mathbf{J}$, and $dA_\perp$ is perpendicular to $\mathbf{J}$, so $|\mathbf{J}|dA_\perp = dI$ gives the current flowing in a given infinitesimal channel along $\mathbf{J}$. We vary $dA_\perp$ inversely with $\mathbf{J}$ along the integration to keep dI constant around the current line. The inductive magnetic energy for one channel over its whole length is then

$$dU^{\rm ind} = \frac{1}{2} dI \int \mathbf{A}\cdot d\boldsymbol{\ell}\ . \quad \text{(B25)}$$

The flux $\Phi_{\rm enc}$ through a closed loop is given by the line integral of the vector potential $\mathbf{A}$ around that loop,

$$\Phi_{\rm enc} = \oint \mathbf{A}\cdot d\boldsymbol{\ell}\ , \quad \text{(B26)}$$

so

$$dU^{\rm ind} = \frac{1}{2} dI \Phi_{\rm enc}\ . \quad \text{(B27)}$$

This enclosed flux arises both from the current in this channel (its self flux, $\Phi_{\rm self}$), and from other currents $\{dI'\}$ in other channels that produce fluxes $\{\Phi'\}$ through this loop. From the definitions of self- and mutual inductances, $\Phi_{\rm self} = \mathcal{L} I$ and $\Phi' = \mathcal{M}_{II'} dI'$, respectively, this enclosed flux can be written

$$\Phi_{\rm enc} = \mathcal{L} dI + dI \int \mathcal{M}_{II'} dI'\ . \quad \text{(B28)}$$

where the integral runs over all other currents dI'. We can then write the total energy in terms of self-inductive and mutual-inductive energies,

$$U = \frac{1}{2}\int dI(\mathcal{L} + \int \mathcal{M}_{II'} dI')\ . \quad \text{(B29)}$$

Equation (B27) implies that the energy in magnetic fields will change when the currents they carry ($\{dI\}$) and the fluxes enclosed by those currents ($\{\Phi_{\rm enc}\}$) change. Equation (B29) relates the field's energy to loops' currents and self inductances ($\{\mathcal{L}\}$, which depend heavily upon their lengths) and mutual inductances ($\{\mathcal{M}\}$, which depend both their lengths and orientations relative to other currents).

We now consider the field energy above a surface on which $B_n \neq 0$ (implying $\mathbf{A}_h \neq 0$ on that surface) and $J_n \neq 0$ (implying $\mathbf{B}_h \neq 0$ on that surface). Because the surface term in Equation (B24) contains $\mathbf{A}$, as a preliminary step, we prove that this the energy does not depend upon choice of gauge. Inserting a gauge term

$\nabla\Lambda$ into Equation (B23) yields

$$\begin{aligned}
\delta U = & \frac{1}{2\mu_0}\int \nabla\Lambda\cdot(\nabla\times\mathbf{B})\,dV + \\
& \frac{1}{2\mu_0}\int \nabla\cdot(\nabla\Lambda\times\mathbf{B})\,dV && \text{(B30)}\\
= & \frac{1}{2\mu_0}\int \nabla\cdot(\Lambda(\nabla\times\mathbf{B}))\,dV + \\
& \frac{1}{2\mu_0}\int \nabla\cdot(\nabla\Lambda\times\mathbf{B})\,dV && \text{(B31)}\\
= & \frac{1}{2\mu_0}\oint [\Lambda(\nabla\times\mathbf{B})+\nabla\Lambda\times\mathbf{B}]\cdot\hat{\mathbf{n}}\,dA && \text{(B32)}\\
= & \frac{1}{2\mu_0}\int [\nabla\times(\Lambda\mathbf{B})]\cdot\hat{\mathbf{n}}\,dA && \text{(B33)}\\
= & \frac{1}{2\mu_0}\oint \Lambda\mathbf{B}_h\cdot d\boldsymbol{\ell} && \text{(B34)}\\
= & 0\ . && \text{(B35)}
\end{aligned}$$

To arrive at Equation (B35), we assumed the area integral in Equation (B33) is over the photosphere, that $\mathbf{B}$ in the integrand vanishes far from an AR's fields, and that the line integral in Equation (B34) is taken far enough from the AR that $\mathbf{B}_h$ is negligible.

If these assumptions are met, then the choice of gauge used in computing the surface term in Equation (B24) does not matter. We remark that this surface term likely changes during flares: the vector potential for a bipolar AR typically points along the PIL (e.g., Chae 2001) (consistent with the right-hand-rule to produce each polarity); the irrotational component of the horizontal field points across the PIL; so $(\mathbf{A}\times\mathbf{B})\cdot\hat{\mathbf{z}}$ is typically nonzero, and $\mathbf{B}_h$ can intensify in flares (as in Figure 7, above). In fact, with $\mathbf{A}$ and the irrotational component of $\mathbf{B}_h$ pointing as one would expect for a generic AR, intensification of this component of $\mathbf{B}_h$ would make $(\mathbf{A}\times\mathbf{B})\cdot\hat{\mathbf{z}}<0$.

When considering the energy of the field above the photosphere in currents that cross this surface, the path integral to determine the enclosed coronal flux goes from one footpoint to its conjugate in the corona, but this does not form a closed loop, so Equation (B26) does not apply. To form a closed loop to determine enclosed coronal flux (presumably the only flux that changes substantially during a flare, given the slow rate of evolution in the interior), one would have to include some path on the photosphere (possibly arbitrary) from a current line's photospheric sink back to its photospheric source, along which the assumption that $d\boldsymbol{\ell}$ was tangent to $\mathbf{J}$, used to derive Equation (B25), would not apply.

REFERENCES

Amari, T., Aly, J., Mikic, Z., & Linker, J. 2010, ApJL, 717, L26

Antiochos, S. K., Karpen, J. T., & DeVore, C. R. 2002, ApJ, 575, 578

Anwar, B., Acton, L. W., Hudson, H. S., Makita, M., McClymont, A. N., & Tsuneta, S. 1993, SoPh, 147, 287

Backus, G. 1986, Reviews of Geophysics, 24, 75

Barczynski, K., Aulanier, G., Janvier, M., Schmieder, B., & Masson, S. 2020, ApJ, 895, 18

Bastian, T., Bain, H., Bradley, R., Chen, B., Dahlin, J., DeLuca, E., Drake, J., Fleishman, G., Gary, D., Glesener, L., Guo, F., Hallinan, G., Hurford, G., Kasper, J., Ji, H., Klimchuk, J., Kobelski, A., Krucker, S., Kuroda, N., Loncope, D., Lonsdale, C., McTiernan, J., Nita, G., Qiu, J., Reeves, K., Saint-Hilaire, P., Schonfeld, S., Shen, C., Tun, S., Wertheimer, D., & White, S. 2019, Astro2020: Decadal Survey on Astronomy and Astrophysics, 2020, 56

Berger, M. A. 1984, Geophys. Astrophys. Fluid Dynamics, 30, 79

Bishop, C. H. 1996, Journal of Atmospheric Sciences, 53, 241

Brosius, J. W. & White, S. M. 2006, ApJL, 641, L69

Chae, J. 2001, ApJ, 560, L95

Chandrasekhar, S. 1961, Hydrodynamic and Hydromagnetic Stability (New York: Dover)

Chintzoglou, G. & Zhang, J. 2013, ApJL, 764, L3

Chintzoglou, G., Zhang, J., Cheung, M. C. M., & Kazachenko, M. 2019, ApJ, 871, 67

DeRosa, M. L., Wheatland, M. S., Leka, K. D., Barnes, G., Amari, T., Canou, A., Gilchrist, S. A., Thalmann, J. K., Valori, G., Wiegelmann, T., Schrijver, C. J., Malanushenko, A., Sun, X., & Régnier, S. 2015, ApJ, 811, 107

Dove, J. B., Gibson, S. E., Rachmeler, L. A., Tomczyk, S., & Judge, P. 2011, ApJL, 731, L1

Fisher, G. H., Welsch, B. T., Abbett, W. P., & Bercik, D. J. 2010, ApJ, 715, 242

Fleck, B., Couvidat, S., & Straus, T. 2011, SoPh, 271, 27

Forbes, T. G. 2000, J. Geophys. Res., 105, 23153

Forbes, T. G. & Isenberg, P. A. 1991, ApJ, 373, 294

Fu, Y. & Welsch, B. T. 2016, SoPh, 291, 383

Gauss, C. F. 1839, 1–52

Gibson, S. E. & Fan, Y. 2006, ApJL, 637, L65

Glassmeier, K. H. & Tsurutani, B. T. 2014, History of Geo- and Space Sciences, 5, 11

Gosain, S. 2012, ApJ, 749, 85

Grad, H. & Rubin, H. 1958, in Proceedings of the 2nd International Conference on Peaceful Uses of Atomic Energy, Vol. 31 (Geneva: United Nations), 190

Hoeksema, J. T., Abbett, W. P., Bercik, D. J., Cheung, M. C. M., DeRosa, M. L., Fisher, G. H., Hayashi, K., Kazachenko, M. D., Liu, Y., Lumme, E., Lynch, B. J., Sun, X., & Welsch, B. T. 2020, ApJS, 250, 28

Hudson, H. S. 2000, ApJL, 531, L75

Hudson, H. S., Fisher, G. H., & Welsch, B. T. 2008, in Astronomical Society of the Pacific Conference Series, Vol. 383, Subsurface and Atmospheric Influences on Solar Activity, ed. R. Howe, R. W. Komm, K. S. Balasubramaniam, & G. J. D. Petrie, 221

Ichimoto, K., Lites, B., Elmore, D., Suematsu, Y., Tsuneta, S., Katsukawa, Y., Shimizu, T., Shine, R., Tarbell, T., Title, A., Kiyohara, J., Shinoda, K., Card, G., Lecinski, A., Streander, K., Nakagiri, M., Miyashita, M., Noguchi, M., Hoffmann, C., & Cruz, T. 2008, SoPh, 249, 233

Jackson, J. D. 1975, Classical Electrodynamics (New York: Wiley)

Kazachenko, M. D., Fisher, G. H., & Welsch, B. T. 2014, ArXiv e-prints: 1404.4027

Kazachenko, M. D., Fisher, G. H., Welsch, B. T., Liu, Y., & Sun, X. 2015, ApJ, 811, 16

Kazachenko, M. D., Lynch, B. J., Welsch, B. T., & Sun, X. 2017, ApJ, 845, 49

Kosovichev, A. G. & Zharkova, V. V. 1999, SoPh, 190, 459

Kosugi, T., Matsuzaki, K., Sakao, T., Shimizu, T., Sone, Y., Tachikawa, S., Hashimoto, T., Minesugi, K., Ohnishi, A., Yamada, T., Tsuneta, S., Hara, H., Ichimoto, K., Suematsu, Y., Shimojo, M., Watanabe, T., Shimada, S., Davis, J. M., Hill, L. D., Owens, J. K., Title, A. M., Culhane, J. L., Harra, L. K., Doschek, G. A., & Golub, L. 2007, SoPh, 243, 3

Kuperus, M. & Raadu, M. A. 1974, A&A, 31, 189

Lantz, S. R. & Fan, Y. 1999, ApJS, 121, 247

Leka, K. D. & Skumanich, A. 1999, SoPh, 188, 3

Lin, H., Kuhn, J. R., & Coulter, R. 2004, ApJL, 613, L177

Lites, B. W., Akin, D. L., Card, G., Cruz, T., Duncan, D. W., Edwards, C. G., Elmore, D. F., Hoffmann, C., Katsukawa, Y., Katz, N., Kubo, M., Ichimoto, K., Shimizu, T., Shine, R. A., Streander, K. V., Suematsu, A., Tarbell, T. D., Title, A. M., & Tsuneta, S. 2013, SoPh, 283, 579

Liu, R., Kliem, B., Török, T., Liu, C., Titov, V. S., Lionello, R., Linker, J. A., & Wang, H. 2012, ApJ, 756, 59

Liu, Y., Welsch, B. T., Valori, G., Georgoulis, M. K., Guo, Y., Pariat, E., Park, S.-H., & Thalmann, J. K. 2022, ApJ, (submitted)

Longcope, D. W. 1996, Solar Phys., 169, 91

Longcope, D. W., McKenzie, D., Cirtain, J., & Scott, J. 2005, ApJ, 630, 596

Low, B. C. & Hundhausen, J. R. 1995, ApJ, 443, 818

Martin, S. F. 1998, Sol. Phys., 182, 107

Mastrano, A., Yang, K. E., & Wheatland, M. S. 2020, SoPh, 295, 97

Melrose, D. B. 1997, ApJ, 486, 521

Metcalf, T. R., Jiao, L., McClymont, A. N., Canfield, R. C., & Uitenbroek, H. 1995, ApJ, 439, 474

Moore, R. L., Hagyard, M. J., & Davis, J. M. 1987, SoPh, 113, 347

Nandy, D., Hahn, M., Canfield, R. C., & Longcope, D. W. 2003, ApJL, 597, L73

Olsen, N., Glassmeier, K. H., & Jia, X. 2010, SSRv, 152, 135

Pesnell, W. D., Thompson, B. J., & Chamberlin, P. C. 2012, SoPh, 275, 3

Petrie, G. J. D. 2012, ArXiv e-prints

Petrie, G. J. D. 2019, ApJS, 240, 11

Priest, E. R. & Forbes, T. G. 2000, Magnetic reconnection: MHD theory and applications (New York: Cambridge University Press)

Rosenbluth, M. N. & Bussac, M. N. 1979, Nuclear Fusion, 19, 489

Sakurai, T. 1981, SoPh, 69, 343

Sammis, I., Tang, F., & Zirin, H. 2000, ApJ, 540, 583

Scherrer, P., Bogart, R. S., Bush, R. I., Hoeksema, J. T., Kosovichev, A., Schou, J., Rosenberg, W., Springer, L., Tarbell, T., Title, A., Wolfson, C., Zayer, I., & The MDI Engineering Team. 1995, Solar Phys., 162, 129

Scherrer, P. H., Schou, J., Bush, R. I., Kosovichev, A. G., Bogart, R. S., Hoeksema, J. T., Liu, Y., Duvall, T. L., Zhao, J., Title, A. M., Schrijver, C. J., Tarbell, T. D., & Tomczyk, S. 2012, SoPh, 275, 207

Schou, J., Scherrer, P. H., Bush, R. I., Wachter, R., Couvidat, S., Rabello-Soares, M. C., Bogart, R. S., Hoeksema, J. T., Liu, Y., Duvall, T. L., Akin, D. J., Allard, B. A., Miles, J. W., Rairden, R., Shine, R. A., Tarbell, T. D., Title, A. M., Wolfson, C. J., Elmore, D. F., Norton, A. A., & Tomczyk, S. 2012, SoPh, 275, 229

Schrijver, C. J., De Rosa, M. L., Metcalf, T., Barnes, G., Lites, B., Tarbell, T., McTiernan, J., Valori, G., Wiegelmann, T., Wheatland, M. S., Amari, T., Aulanier, G., Démoulin, P., Fuhrmann, M., Kusano, K., Régnier, S., & Thalmann, J. K. 2008, ApJ, 675, 1637

Schrijver, C. J., DeRosa, M. L., Title, A. M., & Metcalf, T. R. 2005, ApJ, 628, 501

Schuck, P. W., Chen, J., Schwartz, I. B., & Yurchyshyn, V. 2004, ApJL, 610, L133

Schuck, P. W., Linton, M. G., Knizhnik, K. J., & Leake, J. E. 2022, ApJ, 936, 94

Sezginer, A. & Chew, W. C. 1990, IEEE Transactions on Magnetics, 26, 1137

Shimizu, T., Nagata, S., Tsuneta, S., Tarbell, T., Edwards, C., Shine, R., Hoffmann, C., Thomas, E., Sour, S., Rehse, R., Ito, O., Kashiwagi, Y., Tabata, M., Kodeki, K., Nagase, M., Matsuzaki, K., Kobayashi, K., Ichimoto, K., & Suematsu, Y. 2008, SoPh, 249, 221

Simões, P. J. A., Fletcher, L., Hudson, H. S., & Russell, A. J. B. 2013, ApJ, 777, 152

Sterling, A. C. & Moore, R. L. 2005, ApJ, 630, 1148

Sudol, J. J. & Harvey, J. W. 2005, ApJ, 635, 647

Suematsu, Y., Tsuneta, S., Ichimoto, K., Shimizu, T., Otsubo, M., Katsukawa, Y., Nakagiri, M., Noguchi, M., Tamura, T., Kato, Y., Hara, H., Kubo, M., Mikami, I., Saito, H., Matsushita, T., Kawaguchi, N., Nakaoji, T., Nagae, K., Shimada, S., Takeyama, N., & Yamamuro, T. 2008, SoPh, 249, 197

Swarztrauber, P. & Sweet, R. 1975, Efficient FORTRAN Subprograms for the Solution of Elliptic Partial Differential Equations, NCAR Technical Note NCAR/TN-109+IA, 1975

Tarr, L. & Longcope, D. 2012, ApJ, 749, 64

Taylor, J. B. 1974, Phys. Rev. Lett., 33, 1139

Titov, V. S., Hornig, G., & Démoulin, P. 2002, Journal of Geophysical Research (Space Physics), 107, 1164

Tiwari, S. K., Venkatakrishnan, P., Gosain, S., & Joshi, J. 2009, ApJ, 700, 199

Tomczyk, S., Card, G. L., Darnell, T., Elmore, D. F., Lull, R., Nelson, P. G., Streander, K. V., Burkepile, J., Casini, R., & Judge, P. G. 2008, SoPh, 247, 411

Tsuneta, S., Ichimoto, K., Katsukawa, Y., Nagata, S., Otsubo, M., Shimizu, T., Suematsu, Y., Nakagiri, M., Noguchi, M., Tarbell, T., Title, A., Shine, R., Rosenberg, W., Hoffmann, C., Jurcevich, B., Kushner, G., Levay, M., Lites, B., Elmore, D., Matsushita, T., Kawaguchi, N., Saito, H., Mikami, I., Hill, L. D., & Owens, J. K. 2008, SoPh, 249, 167

Vekstein, G. 2016, Journal of Plasma Physics, 82, 925820401

Wang, H. 1992, SoPh, 140, 85

Wang, H. & Liu, C. 2010, ApJL, 716, L195

Wang, J., Simões, P. J. A., & Fletcher, L. 2018, ApJ, 859, 25

Welsch, B. T. 2015, PASJ, 67, 18

Welsch, B. T. & Fisher, G. H. 2016, SoPh, 291, 1681

Wheatland, M. S. 2007, SoPh, 245, 251

Wheatland, M. S. & Leka, K. D. 2011, ApJ, 728, 112

Wheatland, M. S. & Régnier, S. 2009, ApJL, 700, L88

Wiegelmann, T. 2004, SoPh, 219, 87

Wiegelmann, T. & Sakurai, T. 2012, Living Reviews in Solar Physics, 9, 5

Yeates, A. R. 2017, ApJ, 836, 131